

Efficient and Physically-Consistent Modeling of Reconfigurable Electromagnetic Structures

Alexander Stutz-Tirri, Georg Schwan, and Christoph Studer

Abstract—Reconfigurable electromagnetic structures (REMSs), such as reconfigurable reflectarrays (RRAs) or reconfigurable intelligent surfaces (RISs), hold significant potential to improve wireless communication and sensing systems. Even though several REMS modeling approaches have been proposed in recent years, the literature lacks models that are both computationally *efficient* and *physically consistent*. As a result, algorithms that control the reconfigurable elements of REMSs (e.g., the phase shifts of an RIS) are often built on simplistic models that are inaccurate. To enable physically accurate REMS-parameter tuning, we present a new framework for efficient and physically consistent modeling of *general* REMSs. Our modeling method combines a circuit-theoretic approach with a new formalism that describes a REMS’s interaction with the electromagnetic (EM) waves in its far-field region. Our modeling method enables efficient computation of the entire far-field radiation pattern for *arbitrary* configurations of the REMS reconfigurable elements once a *single* full-wave EM simulation of the non-reconfigurable parts of the REMS has been performed. The predictions made by the proposed framework align with the physical laws of classical electrodynamics and model effects caused by inter-antenna coupling, non-reciprocal materials, polarization, ohmic losses, matching losses, influence of metallic housings, noise from low-noise amplifiers, and noise arising in or received by antennas. In order to validate the efficiency and accuracy of our modeling approach, we (i) compare our modeling method to EM simulations and (ii) conduct a case study involving a planar RRA that enables simultaneous multiuser beam- and null-forming using a new, computationally efficient, and physically accurate parameter tuning algorithm.

Index Terms—Beamforming, circuit theory, full-wave electromagnetic (EM) simulation, interference mitigation, multi-antenna communication, reconfigurable electromagnetic structures (REMS), reflectarrays, reflective surfaces, wireless sensing.

I. INTRODUCTION

RECONFIGURABLE electromagnetic structures (REMSs) have sparked significant interest in the wireless communication and sensing literature over the past years. Prominent instances of REMSs are reconfigurable reflectarrays (RRAs) [1]–[6], reconfigurable array lenses (RALs) [7]–[9], and reconfigurable intelligent surfaces (RISs) [10]–[17]; other, less popular forms of REMSs, also exist; see, e.g., [18]. Moreover, also non-reconfigurable reflectarrays and non-reconfigurable array lenses have experienced a revival in recent years; see, e.g., [19]–[22].

RRAs comprise one or more actively fed antennas and a nearby array of passive but reconfigurable reflecting elements. The reconfigurability of these reflective elements enables dynamic control over the antenna’s behavior, mainly the RRA’s beam pattern, in order to accomplish several goals, such as

maximizing gain, reducing side lobes, or minimizing cross-polarization. RALs consist of arrays of reconfigurable passive elements that function similarly to optical lenses, manipulating electromagnetic (EM) waves passing through the structure to achieve similar goals as RRAs. RISs, which have gained overwhelming popularity in recent years, typically correspond to planar EM structures with reconfigurable elements and are capable of dynamically manipulating their reflecting behavior. Typically, RISs are positioned between transmitter(s) and receiver(s) to dynamically improve the wireless channel for communication or the accuracy of sensing tasks.

The popularity of REMS-related research has led to a significant rise in interest in REMS modeling in an *efficient* and *physically consistent* manner. In what follows, with *efficient* we refer to models (i) whose parameters can be obtained with acceptable computational effort at design time and (ii) that enable real-time prediction of the REMS behavior at manageable complexity; with *physically consistent* we refer to the alignment of the model’s predictions with the physical laws of classical electrodynamics. This includes effects caused by inter-antenna coupling, non-reciprocal materials, polarization, ohmic losses, matching losses, influence of metallic housings, noise from low-noise amplifiers, and noise arising in or received by antennas. While *full-wave EM simulations*¹ can be seen as the gold standard when conducting EM simulations, performing a separate simulation for each configuration of a REMS’s reconfigurable elements is computationally prohibitive, as a single simulation for a specific set of configuration parameters can take hours or even days. For example, high complexity is an issue when modeling RISs, which must be quite large to have a noticeable impact on the propagation conditions. Simulating such large REMSs with conventional full-wave EM simulations demands extensive computational resources (memory as well as CPU time) and is prone to numerical stability issues. Consequently, modeling methods that rely on numerous full-wave EM simulations (e.g., for every possible parameter configuration of an RIS) cannot be considered efficient in the above-mentioned sense.

A. Contributions

Even though a wide variety of efficient REMS modeling approaches has been proposed in recent years, the literature lacks REMS models that are both *efficient* and *physically consistent*. In this paper, we fill this gap by proposing an

The authors are with the Department of Information Technology and Electrical Engineering, ETH Zurich, Switzerland. (email: alstutz@ethz.ch, gschwan@student.ethz.ch, and studer@ethz.ch)

¹Full-wave EM simulations numerically solve all of Maxwell’s equations without any simplifying assumptions. An example of a full-wave EM simulator is Ansys HFSS (short for High-Frequency Structure Simulator) [23].

efficient and physically consistent model for general REMS.² Our main contributions are as follows.

- We propose a new, mathematically rigorous formalism to model an arbitrary REMS's interaction with the (incoming and outgoing) EM waves in its far-field region.
- We propose an *efficient* and *physically-consistent* REMS model by incorporating recent findings on circuit-theoretic models with our REMS-far-field-interaction formalism.
- We show how the model parameters required by our REMS-far-field-interaction formalism can be extracted from a *single* full-wave EM simulation.
- We validate the proposed REMS-far-field-interaction formalism and the method for obtaining the required model parameters in two scenarios by comparing them with Ansys HFSS simulations.
- We demonstrate the efficiency and accuracy of our REMS modeling approach with a case study of a planar RRA with two actively fed antennas that enable simultaneous multiuser beam- and null-forming using a computationally efficient and physics-aware algorithm.
- Finally, we discuss the limitations of our framework and outline potential future avenues.

B. State of the Art

Various REMS models have been proposed in the literature. These models, which are often heuristically motivated, are typically highly efficient but lack either physical consistency or generality; that is, they are only physically consistent for certain specific scenarios. For example, the models discussed in [24]–[28] ignore the REMS's internal coupling and polarization effects; the model used in [29], [30] is based on the assumption that the REMS is composed of identical and periodically arranged unit cells. Similarly, the inhomogeneous sheets of surface impedance model discussed in [31], [32] is only physically consistent if the REMS consists of unit cells with dimensions and inter-cell spacing significantly smaller than the wavelength of interest. In contrast, our REMS model accounts for coupling and polarization effects, and is not limited to REMS that are composed of identical, periodically arranged, or small unit cells.

In [33], Johnson *et al.* proposed a discrete-dipole approximation (DDA)-based model for far-field pattern prediction. Since the DDA decreases the model complexity, this approach is more efficient in predicting a REMS' behavior than a full-wave EM simulation. But there is no free lunch for this approach: the increased efficiency comes at the expense of reduced generality of the model and/or a loss of physical consistency. For example, Diebold *et al.* in [34] use the DDA to model the behavior of an RRA. Specifically, they approximate patch antenna elements with two dipole antennas, achieving high modeling efficiency and physical consistency; however, their model is limited to representing the behavior of the specific patch-antenna-element types used in the paper. In contrast, our

REMS model enables efficient modeling of *general* structures while preserving physical consistency.

In [35], Han *et al.* proposed a coupling-matrix-based REMS model for far-field pattern prediction, which was subsequently utilized by Ji *et al.* in [36]. This coupling-matrix-based modeling approach leverages the linearity of classical electrodynamics to model internal coupling. However, this model is limited to transmitters or receivers, i.e., cannot capture the scattering behavior of a RIS, for example, and cannot predict the power that is absorbed by the coupled antennas. In contrast, our REMS model is able to describe the behavior of RISs and can be used to predict the power absorbed by the (possibly coupled) antennas.

In [37], Wallace and Jensen postulated that wireless communication systems can be represented using circuit theory. In [38], Ivrlač and Nossek demonstrated that circuit-theoretic system models enable both an efficient and physically-consistent modeling of the end-to-end channel between the transmitter power amplifiers (PAs) and the receiver low noise amplifiers (LNAs). In [18], Babakhani *et al.* proposed a circuit-theory-based model for wireless communication systems containing reconfigurable transceivers. In [39], Gradoni and Di Renzo proposed a general circuit-theory-based model for wireless communication systems containing a reconfigurable channel. Further circuit-theory-based models for wireless systems containing REMS can also be found in [40]–[47]. These existing models describe end-to-end wireless channel behavior between the transmitter PAs and the receiver LNAs. Each new physical arrangement of REMSs (e.g., transceivers) requires recalculating the model parameters, which is generally inefficient. In contrast, our model allows each REMS in the system to be characterized separately without first specifying its position and orientation. As we will show, these characterizations can be used to *efficiently* model the system-level behavior of a wireless communication or sensing system with *arbitrarily arranged* REMSs.

In [48], Kerns proposed a mathematical formalism to describe the interaction of a single (non-reconfigurable) antenna with incoming and outgoing EM waves at a reference plane. Kerns modeled the EM waves as plane waves, i.e., he utilized a plane-wave basis³ to describe the incoming and outgoing EM waves. Similarly, Lewis in [49] and Hansen in [50, Ch. 2] demonstrate that the antenna-to-far-field interaction can be formalized by using spherical harmonics as a basis for the far-field EM waves. For a recent reference utilizing a spherical-harmonics-based approach to model antennas, we refer to Shi *et al.* [51]. In contrast to Kerns, Lewis, and Hansen, our proposed REMS-far-field-interaction formalism relies on *spherical waves* as the basis for the incoming and outgoing EM waves. While the choice of basis is strongly application-dependent, our spherical-wave-based formalism offers significant advantages: In contrast to a plane-wave-based approach, our formalism does not require defining a reference plane and therefore naturally facilitates seamless descriptions of the incoming and outgoing EM waves in *all* directions. Additionally, in contrast to a spherical-harmonics-based approach, our formalism avoids computationally complex operations during synthesis (i.e., for

²Conventional single- and multi-antenna transceivers and other *non-reconfigurable* EM systems are special cases of REMS and can therefore also be modeled with our framework.

³In this paper, we use *basis* to refer to the basis of a *linear space*.

calculating the EM wave radiated in a specific direction), such as computing associated Legendre polynomials.

Remark 1 (Spherical Waves). *Although various authors, including Lewis and Hansen, use the term “spherical waves” to refer to spherical harmonics, we use the term “spherical waves” to refer to waves of the form shown in Figure 4. Our terminology allows us to distinguish between the concepts of spherical harmonics and spherical waves and is also commonly used by other authors, such as Nieto-Vesperinas in [52, Sec. 2.1].*

Possibly closest to our work is the modeling approach put forward in [53]–[55]. The authors of these papers use both circuit theory and linear scattering theory to model the behavior of antenna arrays and RISs. However, it is not immediately evident what basis is used to describe the incident EM waves.⁴ Consequently, it remains unclear how models of multiple antenna arrays or RISs can be combined to predict the wireless channel properties. Polarization effects cannot be described by the modeling approach proposed in [53]–[55]; the specific models proposed in [53], [55] are restricted to reciprocal systems; and for the specific model proposed in [54], the rationale behind treating both the incoming and outgoing EM waves as elements in a M -dimensional vector space, where M is the number of RIS elements, is not fully clarified. Furthermore, the authors neither theoretically nor empirically demonstrate that their model is physically consistent, nor do they explain how the model parameters can be obtained in practice. In contrast, (i) we introduce a mathematically rigorous formalism for the REMS far-field interaction derived from first principles, (ii) we demonstrate how multiple REMS models can be combined to predict properties of the wireless channel, (iii) our REMS model can predict polarization effects, and (iv) our model is able to describe the behavior of non-reciprocal systems. Furthermore, we show how the model parameters for our REMS model can be obtained from a *single* full-wave EM simulation, and we numerically validate our model and provide a concrete application example of our framework.

C. Paper Outline

The rest of the paper is organized as follows. In Section II, we introduce our REMS model, including a rigorous mathematical formalism to model the REMS’s interaction with EM waves in its far-field region. Moreover, we discuss aspects of the proposed REMS model such as linear input-output relationships, the calculation of the wireless channel between two REMS, various power metrics, a new gain metric, reciprocity relations, and, finally, the extraction of model parameters from a single full-wave EM simulation. In Section III, we perform simulations to validate (i) the proposed REMS-far-field-interaction formalism and (ii) the method for extracting the necessary model parameters proposed in Section II. In Section IV, we showcase a practical application of our REMS model through a case study featuring a planar RRA and a new and computationally efficient beam- and null-forming algorithm.

⁴While Kerns and Dayhoff [56] are cited, their plane-wave formalism would typically necessitate specifying a reference plane for the space-side waves.

In Section V, we discuss the limitations of the proposed REMS modeling approach. We conclude in Section VI by summarizing the main contributions and discussing potential future avenues. All technical proofs are relegated to Appendix A.

D. Notation

We use boldface and uppercase boldface for general vectors (e.g., \mathbf{a}) and general matrices (e.g., \mathbf{A}), respectively; we use pink sans-serif (e.g., \mathfrak{s}) and pink sans-serif boldface (e.g., \mathfrak{S}) to represent phasors (see Definition 1) and vectors containing phasors, respectively. The superscripts \top and H represent the transpose (e.g., \mathbf{A}^\top) and conjugate transpose (e.g., \mathbf{A}^H), respectively. Given a Hilbert space \mathcal{H} , we use $\langle \mathbf{a}, \mathbf{b} \rangle_{\mathcal{H}}$ to denote the inner product of $\mathbf{a}, \mathbf{b} \in \mathcal{H}$, where we use the convention of linearity in the first argument \mathbf{a} ; to simplify notation, we define the shortcut $[\mathbf{a}]_{\mathbf{b}} \triangleq \langle \mathbf{a}, \mathbf{b} \rangle_{\mathcal{H}}$. The Euclidean norm is denoted with $\|\cdot\|_2$ or $\|\cdot\|_{\mathcal{H}}$. The cross product of two three-dimensional vectors \mathbf{a} and \mathbf{b} is denoted by $\mathbf{a} \times \mathbf{b}$, and the Nabla operator is written as ∇ . We refer to the ℓ th element of the vector \mathbf{a} as \mathbf{a}_ℓ and the element in the ℓ th row and k th column of the matrix \mathbf{A} as $\mathbf{A}_{\ell,k}$. Given a vector \mathbf{a} , we use $\text{diag}(\mathbf{a})$ to denote the diagonal matrix with the elements of \mathbf{a} on its main diagonal. The zero matrix in $\mathbb{C}^{N \times M}$ is denoted with $\mathbf{0}_{N,M}$. To simplify notation, we occasionally omit explicitly specifying the dimension of zero matrices (or vectors). We use blackboard bold font for operators (e.g., \mathfrak{S}). Given $N \in \mathbb{N}$, we define the set $[N] \triangleq \{1, \dots, N\}$. For a set \mathcal{S} , we denote its cardinality by $|\mathcal{S}|$. We denote the Dirac delta by $\delta(\cdot)$ and the Kronecker delta by $\delta_{\ell,k}$, which equals 1 if $\ell = k$ and 0 otherwise. We define the imaginary unit by $j^2 = -1$. For a complex number $z \in \mathbb{C}$, the complex conjugate is \bar{z} , the real part is $\Re\{z\}$, and the imaginary part is $\Im\{z\}$.

To simplify notation, we refrain from explicitly writing physical units, except when specifying numerical values. All physical equations are formulated based on SI units.

II. REMS MODELING METHOD

We now introduce our circuit-theoretical REMS model, whose basic structure is depicted in Figure 1. We then discuss various aspects of the proposed model such as the linear input-output relationships, the calculation of the wireless channel between two REMS, various power metrics, a new gain metric, and reciprocity relationships. Furthermore, we present our approach for extracting model parameters through a *single* full-wave EM simulation.

A. REMS Model Overview

The proposed circuit-theoretic REMS model describes how a REMS interacts with the communication or sensing system in which it is embedded. The REMS can function as a passive structure that manipulates electromagnetic waves, act as a transmitter or a receiver, or operate in any combination of these modes. Our model relies on the following key assumptions.

Assumption 1 (PA and LNA Characteristics). *Each power amplifier (PA; for the transmitters) can be represented with*

an active, noiseless, linear, time-invariant two-port. Each low-noise amplifier (LNA; for the receivers) can be represented with a passive, noisy, linear, time-invariant two-port. (See [57, Sec. 4.1.1] for a definition of noiseless and noisy linear time-invariant two-ports.) Additionally, the output impedances of all PAs and the input impedances of all LNAs have a strictly positive real part.

We are interested in modeling the output stages of $N_{\text{Tx}} \in \mathbb{Z}_{\geq 0}$ PAs and the input stages of $N_{\text{Rx}} \in \mathbb{Z}_{\geq 0}$ LNAs. Assumption 1 implies that these PA output stages and LNA input stages can be modeled with $N = N_{\text{Tx}} + N_{\text{Rx}}$ separate submodels, each with one port⁵. We will henceforth refer to the collection of all those PA and LNA submodels as the *radio-frequency (RF) front-end* of the REMS (see the left-hand side in Figure 1).

Assumption 2 (Radiating Elements Characteristics). *The electromagnetic radiating⁶ elements (e.g., antennas or metallic housing) are fixed at design time and can be represented as a passive, noisy, linear, time-invariant system. Additionally, the connection between the rest of the REMS and the electromagnetically radiating elements can be represented by a finite number of ports. (See, e.g., [57, Sec. 3] for an introduction to noisy linear multiports.)*

Assumption 2 implies that we can model the electromagnetic radiating elements by a separate submodel, which we will henceforth refer to as the *radiating structure* (see the right-hand side in Figure 1). Furthermore, it follows that this submodel represents all interactions of the REMS with its environment, including the (incoming and outgoing) EM waves in the REMS's far-field region. The number of ports connecting the radiating structure with the rest of the REMS model is denoted by $M \in \mathbb{Z}_{\geq 0}$. In general, M can be less than, equal to, or greater than N .

After removing the transmitters, receivers, and radiating structure, we are left with the reconfigurable elements (e.g., phase shifters) and fixed non-radiating structures (e.g., a matching network). We refer to these remaining parts of the REMS as the *tuning network*. For this part, we make the following assumption.

Assumption 3 (Tuning Network Characteristics). *For a fixed configuration of the reconfigurable elements, the tuning network can be modeled as a passive LTI system.*

Assumption 3 implies that, for a fixed configuration of the reconfigurable elements, the tuning network can be modeled as an $N + M$ -port (see the center in Figure 1).

B. REMS Model Details

In the following paragraphs, we provide a detailed description of the proposed REMS model illustrated in Figure 2.

⁵We use *port* to refer to a circuit-theoretic port unless otherwise specified. Analogously, *multiport* refers to a circuit-theoretic multiport.

⁶We use the term *radiating* to refer to structures that interact with their surrounding electromagnetic fields (i.e., electromagnetically non-transparent objects), which also includes purely passive objects.

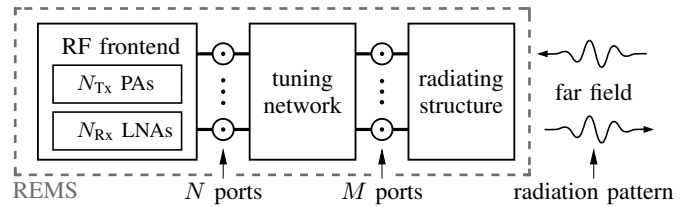


Figure 1. Basic structure of the proposed REMS model. The model is divided into the RF frontend, the tuning network, and the radiating structure. The RF frontend consists of N_{Tx} power amplifiers (PAs) and N_{Rx} low-noise amplifiers (LNAs). The RF frontend is connected to the tuning network via $N = N_{\text{Tx}} + N_{\text{Rx}}$ (circuit-theoretic) ports; and the tuning network is connected to the radiating structure via M ports. The radiating structure models all interactions between the signals at these M ports and the (incoming and outgoing) EM waves in the REMS's far-field region.

1) *Parameterization of Signals and Multiports*: The proposed REMS model is intended for performing narrow-band analyses, i.e., each frequency of interest is analyzed separately. Consequently, for a given analysis frequency, all signals are treated as sinusoidal time functions, which are fully characterized by a phasor.

Definition 1 (Phasor). *For a given sinusoidal time function $s(t) = A \cos(2\pi ft + \phi_0)$, where $t \in \mathbb{R}$ is the time (in seconds), $f \in \mathbb{R}$ the frequency (in Hertz), $A \in \mathbb{R}_{\geq 0}$ is the amplitude, and ϕ_0 the phase, we define this signal's phasor as the complex-valued number given by $\mathbf{s} = \frac{1}{\sqrt{2}} A e^{j\phi_0}$, which represents the root mean square (RMS) value and phase of this signal. We represent phasors with pink sans-serif (e.g., \mathbf{s}) and vectors containing phasors with pink sans-serif boldface (e.g., \mathbf{s}).*

There exists a range of parametrization methods that can be utilized to describe multiports. We use a scattering parameter (S-parameter)-based description for the following reasons: (i) S-parameters are suitable for representing *all* possible linear multiports (including direct connections between ports, short circuits, open circuits, etc.), which is in contrast to other commonly-used descriptions such as those based on impedance (Z-parameters) or admittance (Y-parameters); (ii) A multiport characterized by S-parameters can be directly converted into a signal-flow graph, as demonstrated by Pozar in [58, pp. 194–202], which we will utilize in Section II-C to efficiently derive input-output relationships. For a more detailed discussion on the parametrization of multiports in circuit-theory-based wireless communication models, we refer to Nerini *et al.* in [42].

Following Kurokawa in [59], we define the incoming and outgoing *circuit-theoretic power waves* as follows.

Definition 2 (Circuit-Theoretic Power Waves). *Given a multiport with L ports. For $\ell \in [L]$, we define the circuit-theoretic power wave traveling into the multiport on the ℓ th port as*

$$\mathbf{a}_\ell \triangleq \frac{1}{2\sqrt{R_0}} (\mathbf{v}_\ell + R_0 \mathbf{i}_\ell) \quad (1)$$

and the circuit-theoretic power wave traveling out of the multiport on the ℓ th port as

$$\mathbf{b}_\ell \triangleq \frac{1}{2\sqrt{R_0}} (\mathbf{v}_\ell - R_0 \mathbf{i}_\ell), \quad (2)$$

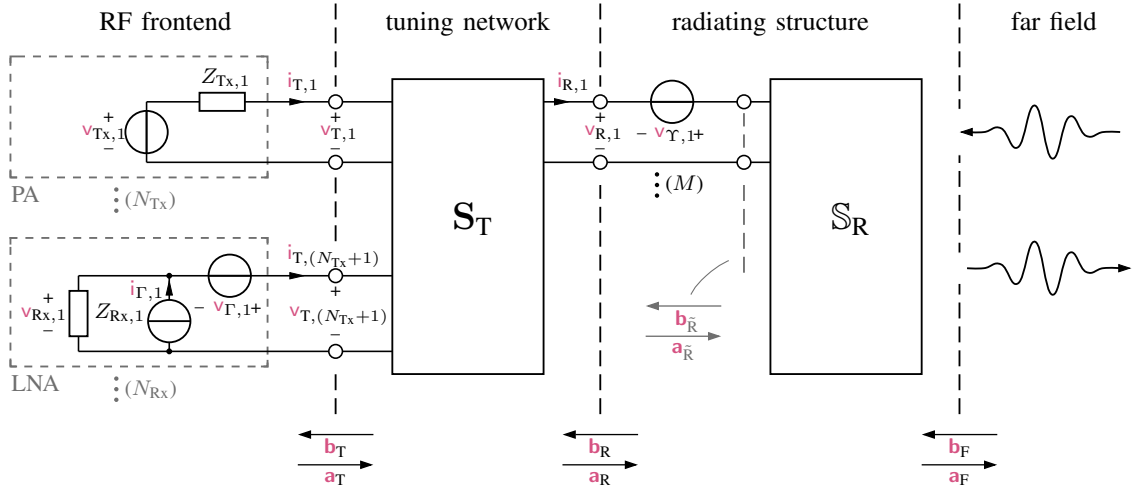


Figure 2. Detailed structure of the proposed REMS model. The *RF frontend* models the power amplifiers (for transmitters) and low noise amplifiers (for receivers). Only the models for the first of a total of N_{Tx} PAs and the first of a total of N_{Rx} LNAs are shown here. The number of (circuit-theoretic) ports connecting the RF frontend with the tuning network is equal to $N = N_{\text{Tx}} + N_{\text{Rx}}$. The *tuning network* represents the reconfigurable elements (e.g., phase shifters) and the fixed non-radiating part (e.g., matching network). The *radiating structure* models the interaction between the REMS's radiating elements (e.g., antennas) and the (incoming and outgoing) EM waves in the REMS's *far-field* region. There are in M ports connecting the tuning network with the radiating structure.

where \mathbf{v}_ℓ and \mathbf{i}_ℓ are the phasors of the voltage and current at port ℓ , respectively. Here, $R_0 \in \mathbb{R}_{>0}$ is an arbitrary reference impedance (50Ω is a commonly-used choice).

2) *RF Frontend*: If the REMS acts as an active transmitter, receiver, or both (i.e., a transceiver), then the RF frontend models the output stage of the PAs and the input stage of the LNAs. For REMSs that do not operate in any of these modes (e.g., a passive RIS), one can omit the RF frontend from the model.

For $\ell \in [N_{\text{Tx}}]$, we represent the output stage of the ℓ th PA by its Thévenin equivalent (see the top-left side of Figure 2), comprising an ideal voltage source and a source impedance $Z_{\text{Tx},\ell}$, where the voltage source is represented by the phasor $\mathbf{v}_{\text{Tx},\ell}$. In our model, we neglect any noise generated in the PAs, as the noise power is typically much lower than that of the amplified signal. Nonetheless, our model could be extended to include noise originating in the PAs.

For $\ell \in [N_{\text{Rx}}]$, we represent the input stage of the ℓ th LNA by its input impedance $Z_{\text{Rx},\ell}$ (see the bottom-left side of Figure 2). Since we assume each LNA behaves as a noisy two-port (of which we only include one port in our model), it is necessary to include two noise sources to model the noise originating from each LNA; see [57, pp. 41–45] for the details. Consequently, for the ℓ th LNA, we model the noise with a current and a voltage source, where these noise sources are represented by the complex-valued random variables $\mathbf{i}_{\Gamma,\ell}$ and $\mathbf{v}_{\Gamma,\ell}$, respectively.

Any potential RF switch or circulator that could be used within a transceiver is not modeled as part of the RF frontend, but rather modeled in the tuning network. We denote the vector of outgoing and incoming power waves (from the RF frontend's perspective) present at the ports that connect the RF frontend with the tuning network as $\mathbf{a}_T \in \mathbb{C}^N$ and $\mathbf{b}_T \in \mathbb{C}^N$, respectively. Moreover, we label the first N_{Tx} elements of \mathbf{a}_T and \mathbf{b}_T as \mathbf{a}_T^{Tx} and \mathbf{b}_T^{Tx} , respectively. Similarly, the remaining N_{Rx} elements are denoted as \mathbf{a}_T^{Rx} and \mathbf{b}_T^{Rx} . To

simplify notation, we define the following vectors and matrices:

$$\mathbf{v}_{\text{Tx}} \triangleq [\mathbf{v}_{\text{Tx},1} \cdots \mathbf{v}_{\text{Tx},N_{\text{Tx}}}]^T, \quad (3)$$

$$\mathbf{v}_{\text{Rx}} \triangleq [\mathbf{v}_{\text{Rx},1} \cdots \mathbf{v}_{\text{Rx},N_{\text{Rx}}}]^T, \quad (4)$$

$$\mathbf{Z}_{\text{Tx}} \triangleq \text{diag}([\mathbf{Z}_{\text{Tx},1} \cdots \mathbf{Z}_{\text{Tx},N_{\text{Tx}}}]^T), \quad (5)$$

$$\mathbf{Z}_{\text{Rx}} \triangleq \text{diag}([\mathbf{Z}_{\text{Rx},1} \cdots \mathbf{Z}_{\text{Rx},N_{\text{Rx}}}]^T), \quad (6)$$

$$\mathbf{v}_{\Gamma} \triangleq [\mathbf{v}_{\Gamma,1} \cdots \mathbf{v}_{\Gamma,N_{\text{Rx}}}]^T, \quad (7)$$

$$\mathbf{i}_{\Gamma} \triangleq [\mathbf{i}_{\Gamma,1} \cdots \mathbf{i}_{\Gamma,N_{\text{Rx}}}]^T. \quad (8)$$

3) *Tuning Network*: The tuning network models the REMS's (i) reconfigurable elements (e.g., phase shifters or switches) and (ii) fixed non-radiating parts (e.g., a matching network). We represent the tuning network by a multiport with a total of $N + M$ ports, which is fully characterized by the scattering matrix $\mathbf{S}_T \in \mathbb{C}^{(N+M) \times (N+M)}$. In particular, it holds that

$$\begin{bmatrix} \mathbf{b}_T \\ \mathbf{a}_R \end{bmatrix} = \underbrace{\begin{bmatrix} \mathbf{S}_{\text{TT}} & \mathbf{S}_{\text{TR}} \\ \mathbf{S}_{\text{RT}} & \mathbf{S}_{\text{RR}} \end{bmatrix}}_{\triangleq \mathbf{S}_T} \begin{bmatrix} \mathbf{a}_T \\ \mathbf{b}_R \end{bmatrix}. \quad (9)$$

Here, $\mathbf{a}_R \in \mathbb{C}^M$ and $\mathbf{b}_R \in \mathbb{C}^M$ represent the outgoing and incoming waves (from the tuning network's perspective) present at the ports connecting the tuning network to the radiating structure, respectively; \mathbf{S}_{TT} is the scattering matrix characterizing the linear dependence of the outgoing waves \mathbf{b}_T on the incoming waves \mathbf{a}_T , etc. As a consequence of assuming the tuning network to be passive, the largest singular value of \mathbf{S}_T cannot exceed 1. If the tuning network is reciprocal, then it also holds that $\mathbf{S}_T^T = \mathbf{S}_T$.

Remark 2. Depending on the REMS and its application, it may be beneficial to further divide the tuning network into subparts. For instance, when modeling a reconfigurable reflectarray (RRA), it might be useful to separate the part of the tuning network that represents the active-feed antennas' matching network from the part that represents the reconfigurable passive electromagnetic elements as illustrated in Figure 12.

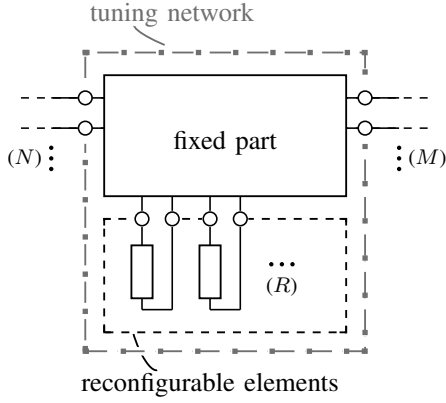


Figure 3. For many scenarios, it makes sense to further separate the tuning network into a static part and a reconfigurable part, as the reconfigurable part can often be represented with a diagonal structure [46].

Remark 3. *Del Hougne recently pointed out in [46] that the actual reconfigurable elements themselves can usually be treated as one-ports (i.e., as general impedances). Therefore, even when the reconfigurable part takes the form of an arbitrary fully connected network (sometimes referred to as a “beyond-diagonal” structure [44]), the actual reconfigurable elements can be represented by $R \in \mathbb{N}$ uncoupled reconfigurable impedances, as shown in Figure 3. Dividing the tuning network into a fixed and a reconfigurable part as shown in Figure 3 might be favorable, as existing algorithms that optimize the REMS’s configuration parameters are often based on the assumption that the reconfigurable elements have such a diagonal structure.*

4) *Radiating Structure and Far Field:* The radiating structure encompasses the radiating elements of the REMS (such as antennas) as well as electromagnetically radiating objects (like metal housings) in its immediate vicinity. Additionally, noise arising in or received by the radiating elements is modeled in this submodel. According to Ivrlač and Nossek [38], extrinsic noise can be included by adding the M voltage sources depicted in Figure 2, which represent the open-circuit noise voltages. It follows from basic circuit theory and Definition 2 that

$$\mathbf{a}_{\tilde{\mathbf{R}}} = \mathbf{a}_{\mathbf{R}} + \frac{1}{2\sqrt{R_0}} \mathbf{v}_{\Upsilon} \quad \text{and} \quad \mathbf{b}_{\tilde{\mathbf{R}}} = \mathbf{b}_{\tilde{\mathbf{R}}} - \frac{1}{2\sqrt{R_0}} \mathbf{v}_{\Upsilon}, \quad (10)$$

where we introduce the noise vector $\mathbf{v}_{\Upsilon} \triangleq [\mathbf{v}_{\Upsilon,1} \dots, \mathbf{v}_{\Upsilon,M}]^T$, formed by the phasors of the extrinsic noise sources.

In order to mathematically describe the electromagnetic waves present in the far field, we use the physicist’s convention for spherical coordinate systems [60], with r as the *radial distance*, θ as the *polar angle*, and φ as the *azimuthal angle*. For each coordinate (r, θ, φ) , we denote the local orthogonal unit vectors in the directions of increasing r , θ , and φ as $\hat{\mathbf{r}}$, $\hat{\boldsymbol{\theta}}$, and $\hat{\boldsymbol{\varphi}}$, respectively. Moreover, we denote the canonical basis vectors as $\hat{\mathbf{x}}$, $\hat{\mathbf{y}}$, and $\hat{\mathbf{z}}$. Using this coordinate system, we define the electrical field phasor vector as

$$\mathbf{E}(r, \theta, \varphi) \triangleq \begin{bmatrix} E_{\hat{\mathbf{x}}}(r, \theta, \varphi) \\ E_{\hat{\mathbf{y}}}(r, \theta, \varphi) \\ E_{\hat{\mathbf{z}}}(r, \theta, \varphi) \end{bmatrix}, \quad (11)$$

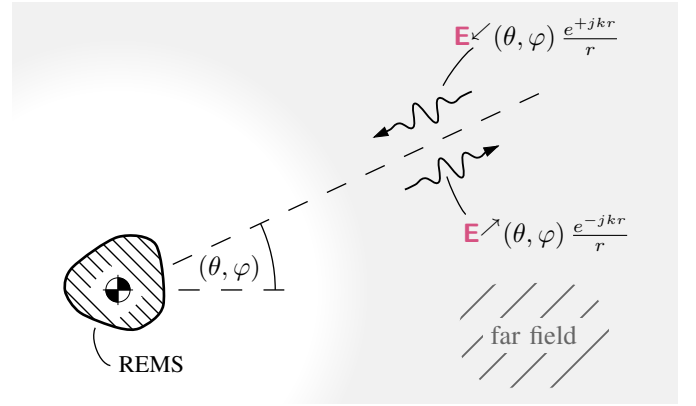


Figure 4. Electromagnetic waves in the REMS’s far-field region, represented as the superposition of incoming (convergent) and outgoing (divergent) spherical waves. The REMS is positioned at the origin of the coordinate system.

where $E_{\hat{\mathbf{x}}}(r, \theta, \varphi)$, $E_{\hat{\mathbf{y}}}(r, \theta, \varphi)$, and $E_{\hat{\mathbf{z}}}(r, \theta, \varphi)$ represent the phasors of the respective components of the electric fields.⁷ As demonstrated by Nieto-Vesperinas in [52, Eq. 5.12], far away from the REMS, in particular as $r \rightarrow \infty$, we have

$$\lim_{r \rightarrow \infty} \mathbf{E}(r, \theta, \varphi) = \mathbf{E}^{\leftarrow}(\theta, \varphi) \frac{e^{+jkr}}{r} + \mathbf{E}^{\rightarrow}(\theta, \varphi) \frac{e^{-jkr}}{r}. \quad (12)$$

Here, $k \triangleq f\sqrt{\mu_0\epsilon_0}$ is the free-space wavenumber, μ_0 is the free-space permeability, and ϵ_0 is the free-space permittivity. Furthermore, $\mathbf{E}^{\leftarrow}(\theta, \varphi)$ and $\mathbf{E}^{\rightarrow}(\theta, \varphi)$ are complex-valued three-dimensional vectors that do not depend on the radial distance r . Equation (12) can be interpreted as the superposition of an incoming *convergent spherical wave* and an outgoing *divergent spherical wave*, as illustrated in Figure 4. Here, $\mathbf{E}^{\leftarrow}(\theta, \varphi)$ and $\mathbf{E}^{\rightarrow}(\theta, \varphi)$ represent the parts of the respective electric field phasor vectors that do not depend on r . Because we analyze the electromagnetic field in free space, far from any source, it follows directly from the free-space Maxwell’s equations that (i) the complete electromagnetic field is fully characterized by the electric field and (ii) the electric field components in the propagation direction are zero:

$$[\mathbf{E}^{\leftarrow}(\theta, \varphi)]_{\hat{\mathbf{r}}} = [\mathbf{E}^{\rightarrow}(\theta, \varphi)]_{\hat{\mathbf{r}}} = 0 \text{ V}. \quad (13)$$

Here, we use the shorthand notation $[\mathbf{a}]_{\mathbf{u}} \triangleq \langle \mathbf{a}, \mathbf{u} \rangle_{\mathbb{C}^3}$. As a consequence, the electromagnetic fields in the REMS far-field region are fully characterized by the *far-field power wave patterns* introduced in Definition 3, which are elements of a Hilbert space, as shown in Proposition 1. A proof of Proposition 1 can be found in Appendix A-A.

Definition 3 (Far-field Power Wave Patterns). *Let $\Omega \triangleq [0, \pi] \times [0, 2\pi)$. We define the outgoing far-field power wave pattern*

$$\mathbf{a}_{\mathbf{F}} : \Omega \rightarrow \mathbb{C}^2, (\theta, \varphi) \mapsto \frac{1}{\sqrt{Z_0}} \begin{bmatrix} [\mathbf{E}^{\rightarrow}(\theta, \varphi)]_{\hat{\boldsymbol{\theta}}} \\ [\mathbf{E}^{\rightarrow}(\theta, \varphi)]_{\hat{\boldsymbol{\varphi}}} \end{bmatrix} \quad (14)$$

and the incoming far-field power wave pattern

$$\mathbf{b}_{\mathbf{F}} : \Omega \rightarrow \mathbb{C}^2, (\theta, \varphi) \mapsto \frac{1}{\sqrt{Z_0}} \begin{bmatrix} [\mathbf{E}^{\leftarrow}(\theta, \varphi)]_{\hat{\boldsymbol{\theta}}} \\ [\mathbf{E}^{\leftarrow}(\theta, \varphi)]_{\hat{\boldsymbol{\varphi}}} \end{bmatrix}, \quad (15)$$

⁷Note that by using capital letters for the electric field, we deviate from our usual notation. We do this because it is the convention to represent the electric field with the capital letter E.

where $Z_0 \triangleq \sqrt{\mu_0/\epsilon_0}$ is the free-space impedance.

Remark 4 (Polarization). *The far-field power wave patterns introduced in Definition 3 fully describe the far-field polarization. To see this, it is insightful to interpret $\mathbf{a}_F(\theta, \varphi)$ and $\mathbf{b}_F(\theta, \varphi)$ as the (with $\frac{r}{\sqrt{Z_0}}$ scaled) Jones vectors [61], [62, pp. 334–341] of the (approximately plane) waves present at (r, θ, φ) .*

Proposition 1. *We use P^\nearrow to denote the power radiated into the far-field region and P^\swarrow to denote the power incoming from the far-field region. If both P^\swarrow and P^\nearrow are finite, then the outgoing far-field power wave pattern \mathbf{a}_F and the incoming far-field power wave pattern \mathbf{b}_F are elements of the Hilbert space⁸ L^2 , induced by the functions $\mathbf{t} : \Omega \rightarrow \mathbb{C}^2$ that satisfy*

$$\|\mathbf{t}\|_{L^2}^2 \triangleq \iint_{\Omega} \|\mathbf{t}(\theta, \varphi)\|^2 \sin(\theta) d(\theta, \varphi) < \infty. \quad (16)$$

Specifically, it follows that $\mathbf{a}_F, \mathbf{b}_F \in L^2$.

Remark 5. *For $(\theta, \varphi) \in \Omega$, it is easy to show that $\|\mathbf{a}_F(\theta, \varphi)\|_2^2$ and $\|\mathbf{b}_F(\theta, \varphi)\|_2^2$ correspond to the transmitted and received radiation intensity $I(\theta, \varphi)$, respectively, i.e., the transmitted/received power per unit solid angle.*

We have derived that the interface variables of the radiating structure are the circuit-theoretic power waves $\mathbf{a}_{\bar{R}}, \mathbf{b}_{\bar{R}} \in \mathbb{C}^M$ at the interface towards the tuning network, and the far-field power wave patterns $\mathbf{a}_F, \mathbf{b}_F \in L^2$ at the interface to the far field and the rest of the system in which the REMS is embedded. It follows from the linearity of Maxwell's equations that the outgoing (from the radiating structure's perspective) power waves $\mathbf{b}_{\bar{R}}$ and \mathbf{a}_F are related to the incoming power waves $\mathbf{a}_{\bar{R}}$ and \mathbf{b}_F as follows:

$$\begin{bmatrix} \mathbf{b}_{\bar{R}} \\ \mathbf{a}_F \end{bmatrix} = \underbrace{\begin{bmatrix} \mathbb{S}_{\text{RRR}} & \mathbb{S}_{\text{RFF}} \\ \mathbb{S}_{\text{RFR}} & \mathbb{S}_{\text{FFF}} \end{bmatrix}}_{\triangleq \mathbb{S}_{\text{R}}} \begin{bmatrix} \mathbf{a}_{\bar{R}} \\ \mathbf{b}_F \end{bmatrix}. \quad (17)$$

Here, the four ‘‘submatrices’’ of \mathbb{S}_{R} are bounded⁹ linear operators, which we specify next.

The *inter-element coupling operator* $\mathbb{S}_{\text{RRR}} : \mathbb{C}^M \rightarrow \mathbb{C}^M$ can simply be represented by the matrix $\mathbf{S}_{\text{RRR}} \in \mathbb{C}^{M \times M}$.

The *transmitting operator* $\mathbb{S}_{\text{RFR}} : \mathbb{C}^M \rightarrow L^2$ is a finite-rank operator with rank not larger than M . Hence, its action on $\mathbf{s} \in \mathbb{C}^M$ can be represented as

$$(\mathbb{S}_{\text{RFR}} \mathbf{s})(\theta, \varphi) = \sum_{m \in [M]} \mathbf{s}_{\text{RFR}}(m; \theta, \varphi) [\mathbf{s}]_m, \quad (18)$$

where for $\Omega \triangleq [0, \pi] \times [0, 2\pi]$ the kernel $\mathbf{s}_{\text{RFR}} : [M] \times \Omega \rightarrow \mathbb{C}^2$ fully characterizes the operator. See Appendix A-D for a formal proof that \mathbb{S}_{RFR} can be represented as in (18).

⁸To be specific, the space we use here, is the L^2 -space induced by the measure space $(\Omega, \mathcal{A}, \mu)$ and the Hilbert space \mathbb{C}^2 , where \mathcal{A} is the respective σ -algebra of Lebesgue measurable sets, μ is the measure defined by $\mu : \mathcal{A} \rightarrow [0, \infty]$, $X \mapsto \iint_{(\theta, \varphi) \in X} \sin(\theta) d\theta d\varphi$.

⁹Boundedness follows from realizing that the Euclidean norms of $\mathbf{b}_{\bar{R}}, \mathbf{a}_{\bar{R}} \in \mathbb{C}^M$ and the L^2 -norms of $\mathbf{b}_F, \mathbf{a}_F \in L^2$ represent the power transported by these waves as shown in the proof of Proposition 1.

The *receiving operator* $\mathbb{S}_{\text{RRF}} : L^2 \rightarrow \mathbb{C}^M$ is, similarly to the transmitting operator, a finite-rank operator whose action on a function $\mathbf{t} \in L^2$ can be represented as

$$[\mathbb{S}_{\text{RRF}} \mathbf{t}]_m = \langle \mathbf{t}, \bar{\mathbf{s}}_{\text{RRF}}(m; \cdot) \rangle_{L^2} \quad (19)$$

$$= \iint_{\Omega} \langle \mathbf{t}(\theta, \varphi), \bar{\mathbf{s}}_{\text{RRF}}(m; \theta, \varphi) \rangle_{\mathbb{C}^2} \sin(\theta) d(\theta, \varphi). \quad (20)$$

Here, we use (i) the kernel $\mathbf{s}_{\text{RRF}} : [M] \times \Omega \rightarrow \mathbb{C}^2$ to fully characterize the operator, (ii) the notation $\bar{\mathbf{s}}_{\text{RRF}}(m; \cdot)$ to represent an element in the previously introduced L^2 -space, induced by the (complex conjugated) kernel and the respective index m , and (iii) the inner product of the same L^2 -space. See Appendix A-E for a formal proof that \mathbb{S}_{RRF} can be represented as in (20).

The *scattering operator* $\mathbb{S}_{\text{RFF}} : L^2 \rightarrow L^2$ can, according to Saxon [63, Eq. 4], be represented by a surface-integral over the unit sphere S^2 as

$$(\mathbb{S}_{\text{RFF}} \mathbf{t})(\hat{\mathbf{r}}) = \iint_{S^2} \mathbf{S}_{\text{RFF}}(\hat{\mathbf{r}}; \hat{\mathbf{r}}') \mathbf{t}(\hat{\mathbf{r}}') d\mathbf{S}'. \quad (21)$$

Here, $\hat{\mathbf{r}}$ and $\hat{\mathbf{r}}'$ are unit vectors corresponding to spherical coordinates (θ, φ) and (θ', φ') , respectively.¹⁰ Furthermore, $d\mathbf{S}'$ denotes the differential vector element of surface area normal to the unit sphere S^2 at position $\hat{\mathbf{r}}'$ and the kernel \mathbf{S}_{RFF} fully characterizes this scattering operator. This kernel \mathbf{S}_{RFF} can, for example, be a proper function of the form $\Omega \times \Omega \rightarrow \mathbb{C}^{2 \times 2}$. In this special case one can directly parametrize the integral in (21) by (θ, φ) and write

$$\begin{aligned} (\mathbb{S}_{\text{RFF}} \mathbf{t})(\theta, \varphi) &= \iint_{\Omega} \mathbf{S}_{\text{RFF}}(\theta, \varphi; \theta', \varphi') \mathbf{t}(\theta', \varphi') \sin(\theta') d(\theta', \varphi'). \end{aligned} \quad (22)$$

Note that more general mathematical tools, such as distributions, might be necessary to describe the kernel \mathbf{S}_{RFF} , e.g., if no scatterer is present and \mathbb{S}_{RFF} acts as the identity operator.

C. Input-Output Relationships

We now derive several input-output relationships for a REMS. We begin by mathematically describing the behavior of the RF frontend. From basic circuit theory and Definition 2, it follows that the PAs behavior can be described by

$$\begin{aligned} \mathbf{a}_{\text{T}}^{\text{Tx}} &= \underbrace{(\mathbf{Z}_{\text{Tx}} + R_0 \mathbf{I}_{N_{\text{Tx}}})^{-1} (\mathbf{Z}_{\text{Tx}} - R_0 \mathbf{I}_{N_{\text{Tx}}})}_{\triangleq \mathbf{S}_{\text{RF}}^{\text{Tx}}} \mathbf{b}_{\text{T}}^{\text{Tx}} \\ &+ \underbrace{(\mathbf{Z}_{\text{Tx}} + R_0 \mathbf{I}_{N_{\text{Tx}}})^{-1} \sqrt{R_0}}_{\triangleq \tilde{\mathbf{K}}_{\text{vTx}}} \mathbf{v}_{\text{Tx}}, \end{aligned} \quad (23)$$

where we define $\mathbf{S}_{\text{RF}}^{\text{Tx}}$ and $\tilde{\mathbf{K}}_{\text{vTx}}$ to simplify notation later.¹¹ Analogously, one can show that for the LNAs it holds that

$$\mathbf{a}_{\text{T}}^{\text{Rx}} = \underbrace{(\mathbf{Z}_{\text{Rx}} + R_0 \mathbf{I}_{N_{\text{Rx}}})^{-1} (\mathbf{Z}_{\text{Rx}} - R_0 \mathbf{I}_{N_{\text{Rx}}})}_{\triangleq \mathbf{S}_{\text{RF}}^{\text{Rx}}} \mathbf{b}_{\text{T}}^{\text{Rx}}$$

¹⁰To ensure correct notation, functions that map the unit vectors $\hat{\mathbf{r}}$ and $\hat{\mathbf{r}}'$ to their respective spherical coordinates would need to be added in (21). However, we do not explicitly include these functions in the equation to simplify notation.

¹¹It follows from the structure of the RF frontend in Figure 2 and Assumption 1 that the impedance matrices \mathbf{Z}_{Tx} and \mathbf{Z}_{Rx} are non-negative diagonal matrices. Consequently, all inverses in equations (23), (24), and (25) exist as long as one chooses a strictly positive reference resistance (e.g., $R_0 = 50 \Omega$).

$$\begin{aligned}
& + \underbrace{(\mathbf{Z}_{\text{Rx}} + R_0 \mathbf{I}_{N_{\text{Rx}}})^{-1} \sqrt{R_0} \mathbf{Z}_{\text{Rx}}}_{\triangleq \tilde{\mathbf{K}}_{\text{i}_\Gamma}} \mathbf{i}_\Gamma, \\
& + \underbrace{(\mathbf{Z}_{\text{Rx}} + R_0 \mathbf{I}_{N_{\text{Rx}}})^{-1} \sqrt{R_0}}_{\triangleq \tilde{\mathbf{K}}_{\mathbf{v}_\Gamma}} \mathbf{v}_\Gamma
\end{aligned} \quad (24)$$

$$\mathbf{v}_{\text{Rx}} = \underbrace{(\sqrt{R_0})^{-1} \mathbf{Z}_{\text{Rx}}}_{\triangleq \tilde{\mathbf{K}}_{\mathbf{v}_{\text{Rx}}}} (\mathbf{b}_T^{\text{Rx}} - \mathbf{a}_T^{\text{Rx}}) + \mathbf{Z}_{\text{Rx}} \mathbf{i}_\Gamma, \quad (25)$$

where we define $\mathbf{S}_{\text{RF}}^{\text{Rx}}$, $\tilde{\mathbf{K}}_{\mathbf{v}_{\text{Rx}}}$, $\tilde{\mathbf{K}}_{\text{i}_\Gamma}$, and $\tilde{\mathbf{K}}_{\mathbf{v}_\Gamma}$ to simplify notation later. To further simplify notation, we introduce the following auxiliary matrices:

$$\mathbf{K}_{\mathbf{v}_{\text{Tx}}} \triangleq \begin{bmatrix} \tilde{\mathbf{K}}_{\mathbf{v}_{\text{Tx}}} \\ \mathbf{0}_{N_{\text{Rx}}, N_{\text{Tx}}} \end{bmatrix}, \quad \mathbf{K}_{\mathbf{v}_\Gamma} \triangleq \begin{bmatrix} \mathbf{0}_{N_{\text{Tx}}, N_{\text{Rx}}} \\ \tilde{\mathbf{K}}_{\mathbf{v}_\Gamma} \end{bmatrix}, \quad \mathbf{K}_{\text{i}_\Gamma} \triangleq \begin{bmatrix} \mathbf{0}_{N_{\text{Tx}}, N_{\text{Rx}}} \\ \tilde{\mathbf{K}}_{\text{i}_\Gamma} \end{bmatrix}, \quad (26)$$

$$\mathbf{K}_{\mathbf{v}_{\text{Rx}}} \triangleq \begin{bmatrix} \mathbf{0}_{N_{\text{Rx}}, N_{\text{Tx}}} & \tilde{\mathbf{K}}_{\mathbf{v}_{\text{Rx}}} \\ \mathbf{S}_{\text{RF}}^{\text{Tx}} & \mathbf{0}_{N_{\text{Tx}}, N_{\text{Rx}}} \end{bmatrix}, \quad \mathbf{S}_{\text{RF}} \triangleq \begin{bmatrix} \mathbf{S}_{\text{RF}}^{\text{Tx}} & \mathbf{0}_{N_{\text{Tx}}, N_{\text{Rx}}} \\ \mathbf{0}_{N_{\text{Rx}}, N_{\text{Tx}}} & \mathbf{S}_{\text{RF}}^{\text{Rx}} \end{bmatrix}. \quad (27)$$

The REMS's behavior can be described by the system of linear equations consisting of (9), (10), (17), (23), (24), (25), (26), and (27). Alternatively, this system of equations can be visualized as the signal-flow graph depicted in Figure 5. Visualizing the REMS's behavior with such a signal-flow graph offers the advantage that the various input-output relationships can be derived quickly. For example, the return loop method introduced by Riegle and Lin in [64] can be used to derive input-output relationships. The inputs to our REMS model include the signal and noise source voltages and currents \mathbf{v}_{Tx} , \mathbf{v}_Γ , \mathbf{i}_Γ , \mathbf{v}_Υ , and the incoming far-field power wave pattern \mathbf{b}_F , while the outputs of the model are the LNA receive voltage vector \mathbf{v}_{Rx} and the outgoing far-field power wave pattern \mathbf{a}_F .

For an output \mathbf{s}_{out} and an input \mathbf{s}_{in} , we denote the operator characterizing the linear dependence of \mathbf{s}_{out} on \mathbf{s}_{in} as $\mathbb{G}_{\mathbf{s}_{\text{in}}}^{\mathbf{s}_{\text{out}}}$. $\mathbb{G}_{\mathbf{s}_{\text{in}}}^{\mathbf{s}_{\text{out}}}$ is implicitly defined by

$$\mathbf{s}_{\text{out}} \Big|_{\text{inputs other than } \mathbf{s}_{\text{in}} \text{ are disabled}} = \mathbb{G}_{\mathbf{s}_{\text{in}}}^{\mathbf{s}_{\text{out}}} \mathbf{s}_{\text{in}}, \quad (28)$$

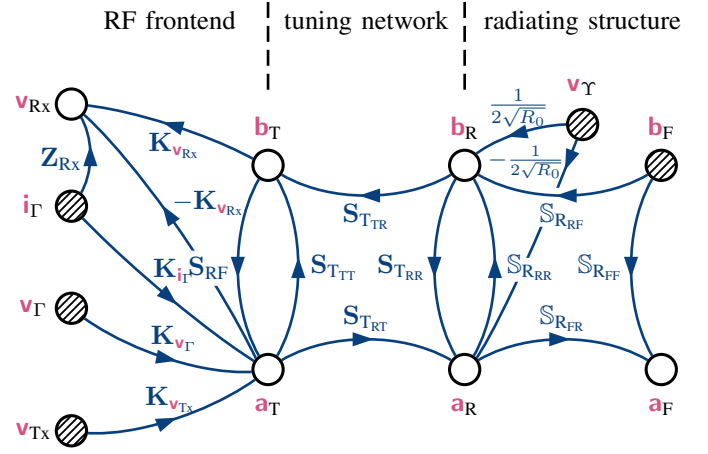


Figure 5. Signal-flow graph of our model: The nodes represent (i) complex vectors that correspond to voltages, currents, and circuit theoretic power waves, or (ii) elements in an L^2 -space, which represent the far-field radiation pattern of the incoming and outgoing waves. The edges of the graph represent bounded linear operators between the respective spaces. To enhance readability, the nodes representing inputs are hatched.

where the vertical bar $|$ means “evaluated at.” Using this notation one can write

$$\mathbf{a}_F = \mathbb{G}_{\mathbf{v}_{\text{Tx}}}^{\mathbf{a}_F} \mathbf{v}_{\text{Tx}} + \mathbb{G}_{\mathbf{b}_F}^{\mathbf{a}_F} \mathbf{b}_F + \mathbb{G}_{\mathbf{v}_\Gamma}^{\mathbf{a}_F} \mathbf{v}_\Gamma + \mathbb{G}_{\text{i}_\Gamma}^{\mathbf{a}_F} \mathbf{i}_\Gamma + \mathbb{G}_{\mathbf{v}_\Upsilon}^{\mathbf{a}_F} \mathbf{v}_\Upsilon \quad (29)$$

$$\mathbf{v}_{\text{Rx}} = \mathbb{G}_{\mathbf{v}_{\text{Tx}}}^{\mathbf{v}_{\text{Rx}}} \mathbf{v}_{\text{Tx}} + \mathbb{G}_{\mathbf{b}_F}^{\mathbf{v}_{\text{Rx}}} \mathbf{b}_F + \mathbb{G}_{\mathbf{v}_\Gamma}^{\mathbf{v}_{\text{Rx}}} \mathbf{v}_\Gamma + \mathbb{G}_{\text{i}_\Gamma}^{\mathbf{v}_{\text{Rx}}} \mathbf{i}_\Gamma + \mathbb{G}_{\mathbf{v}_\Upsilon}^{\mathbf{v}_{\text{Rx}}} \mathbf{v}_\Upsilon. \quad (30)$$

In (31)–(37), we explicitly show how most of the linear operators appearing in (29) and (30) can be constructed from model parameters; the auxiliary matrices \mathbf{L}_1 to \mathbf{L}_7 are defined in (38) to (44), respectively. We refrain from giving constructing formulas for $\mathbb{G}_{\mathbf{v}_{\text{Tx}}}^{\mathbf{a}_F}$, $\mathbb{G}_{\text{i}_\Gamma}^{\mathbf{a}_F}$, and $\mathbb{G}_{\mathbf{v}_\Upsilon}^{\mathbf{a}_F}$, because the influence of noise on the outgoing far-field power wave pattern \mathbf{a}_F can typically be ignored.

$$\mathbb{G}_{\mathbf{v}_{\text{Tx}}}^{\mathbf{a}_F} = \mathbb{S}_{\text{RFR}} (\mathbf{I}_M - \mathbf{L}_2)^{-1} \mathbf{S}_{\text{TRT}} (\mathbf{I}_N - \mathbf{L}_1 - \mathbf{L}_3)^{-1} \mathbf{K}_{\mathbf{v}_{\text{Tx}}} \quad (31)$$

$$\mathbb{G}_{\mathbf{b}_F}^{\mathbf{a}_F} = \mathbb{S}_{\text{RFR}} (\mathbf{S}_{\text{TRT}} \mathbf{S}_{\text{RF}} (\mathbf{I}_N - \mathbf{L}_5)^{-1} \mathbf{S}_{\text{TR}} + \mathbf{S}_{\text{TRR}}) (\mathbf{I}_M - \mathbf{L}_6 - \mathbf{L}_7)^{-1} \mathbb{S}_{\text{RFR}} + \mathbb{S}_{\text{RFF}} \quad (32)$$

$$\mathbb{G}_{\mathbf{v}_{\text{Tx}}}^{\mathbf{v}_{\text{Rx}}} = \mathbf{K}_{\mathbf{v}_{\text{Rx}}} (\mathbf{S}_{\text{TR}} \mathbb{S}_{\text{RR}} (\mathbf{I}_M - \mathbf{L}_2)^{-1} \mathbf{S}_{\text{TRT}} + \mathbf{S}_{\text{TT}} - \mathbf{I}_N) (\mathbf{I}_N - \mathbf{L}_1 - \mathbf{L}_3)^{-1} \mathbf{K}_{\mathbf{v}_{\text{Tx}}} \quad (33)$$

$$\mathbb{G}_{\mathbf{v}_\Gamma}^{\mathbf{v}_{\text{Rx}}} = \mathbf{K}_{\mathbf{v}_{\text{Rx}}} (\mathbf{S}_{\text{TR}} \mathbb{S}_{\text{RR}} (\mathbf{I}_M - \mathbf{L}_2)^{-1} \mathbf{S}_{\text{TRT}} + \mathbf{S}_{\text{TT}} - \mathbf{I}_N) (\mathbf{I}_N - \mathbf{L}_1 - \mathbf{L}_3)^{-1} \mathbf{K}_{\mathbf{v}_\Gamma} \quad (34)$$

$$\mathbb{G}_{\text{i}_\Gamma}^{\mathbf{v}_{\text{Rx}}} = \mathbf{K}_{\mathbf{v}_{\text{Rx}}} (\mathbf{S}_{\text{TR}} \mathbb{S}_{\text{RR}} (\mathbf{I}_M - \mathbf{L}_2)^{-1} \mathbf{S}_{\text{TRT}} + \mathbf{S}_{\text{TT}} - \mathbf{I}_N) (\mathbf{I}_N - \mathbf{L}_1 - \mathbf{L}_3)^{-1} \mathbf{K}_{\text{i}_\Gamma} + \mathbf{Z}_{\text{Rx}} \quad (35)$$

$$\mathbb{G}_{\mathbf{b}_F}^{\mathbf{v}_{\text{Rx}}} = \mathbf{K}_{\mathbf{v}_{\text{Rx}}} (\mathbf{I}_N - \mathbf{S}_{\text{RF}}) (\mathbf{I}_N - \mathbf{L}_5)^{-1} \mathbf{S}_{\text{TR}} (\mathbf{I}_M - \mathbf{L}_6 - \mathbf{L}_7)^{-1} \mathbb{S}_{\text{RFR}} \quad (36)$$

$$\mathbb{G}_{\mathbf{v}_\Upsilon}^{\mathbf{v}_{\text{Rx}}} = \mathbf{K}_{\mathbf{v}_{\text{Rx}}} (\mathbf{I}_N - \mathbf{S}_{\text{RF}}) (\mathbf{I}_N - \mathbf{L}_5)^{-1} \mathbf{S}_{\text{TR}} (\mathbf{I}_M - \mathbf{L}_6 - \mathbf{L}_7)^{-1} (\mathbf{I}_M - \mathbb{S}_{\text{RR}}) \frac{1}{2\sqrt{R_0}} \quad (37)$$

$$\mathbf{L}_1 \triangleq \mathbf{S}_{\text{RF}} \mathbf{S}_{\text{TT}} \quad (38)$$

$$\mathbf{L}_2 \triangleq \mathbf{S}_{\text{TR}} \mathbb{S}_{\text{RR}} \quad (39)$$

$$\mathbf{L}_3 \triangleq \mathbf{S}_{\text{RF}} \mathbf{S}_{\text{TR}} \mathbb{S}_{\text{RR}} (\mathbf{I}_M - \mathbf{L}_2)^{-1} \mathbf{S}_{\text{TRT}} \quad (40)$$

$$\mathbf{L}_4 \triangleq \mathbf{S}_{\text{TRT}} \mathbf{S}_{\text{RF}} (\mathbf{I}_N - \mathbf{L}_5)^{-1} \mathbf{S}_{\text{TR}} \mathbb{S}_{\text{RR}} \quad (41)$$

$$\mathbf{L}_5 \triangleq \mathbf{S}_{\text{TT}} \mathbf{S}_{\text{RF}} \quad (42)$$

$$\mathbf{L}_6 \triangleq \mathbb{S}_{\text{RR}} \mathbf{S}_{\text{TR}} \quad (43)$$

$$\mathbf{L}_7 \triangleq \mathbb{S}_{\text{RR}} \mathbf{S}_{\text{TRT}} \mathbf{S}_{\text{RF}} (\mathbf{I}_N - \mathbf{L}_5)^{-1} \mathbf{S}_{\text{TR}}. \quad (44)$$

D. Wireless Channel Between Two REMSs

In Section II-C, we have demonstrated how various input-output relationships of a single REMS can be calculated using our REMS model. However, it is often necessary to derive the input-output relationships for the entire communication system. Motivated by this, we will now present a simple example to illustrate how the models of two REMSs can be combined to determine the wireless channel between them.

We consider a scenario with two REMSs placed far apart in empty space. The first REMS, acting as the transmitter, is equipped with $M^{(1)}$ antennas, while the second REMS, serving as the receiver, is equipped with $M^{(2)}$ antennas. In our scenario, we are interested in calculating the in Definition 4 introduced *transmission coefficients* of the wireless channel between the two REMS. We now introduce Proposition 2. A proof of Proposition 2 can be found in Appendix A-B.

Definition 4 (Transmission Coefficient of a Wireless Channel). *Given a system consisting of U REMSs, for which Assumption 2 holds. One can treat the subsystem consisting of the radiating structures of these U REMSs and the wireless channel between them as a multiport with $\sum_{u \in [U]} M^{(u)}$ ports, analogous to the multiport Z_A in [38, Fig. 2]). For $u^{(1)}, u^{(2)} \in [U]$ and $\ell^{(1)} \in M^{(u^{(1)})}$, $\ell^{(2)} \in M^{(u^{(2)})}$, we define the scattering parameter that characterizes the scattering from the incoming circuit-theoretic power wave $[\mathbf{a}_{\hat{R}}^{(u^{(1)})}]_{\ell^{(1)}}$ at the $\ell^{(1)}$ th port of REMS $u^{(1)}$ to the outgoing circuit-theoretic power wave $[\mathbf{b}_{\hat{R}}^{(u^{(2)})}]_{\ell^{(2)}}$ at the $\ell^{(2)}$ th port of REMS $u^{(2)}$ as the transmission coefficient $S_{u_{\ell^{(2)}}^{(2)} u_{\ell^{(1)}}^{(1)}}$.*

Proposition 2. *Given two REMSs, each with finite spatial support, for which Assumption 2 hold. Assume that they are placed in empty space and their radiating structures possess $M^{(1)}$ and $M^{(2)}$ ports, respectively. Additionally, assume that the kernels $\mathbf{s}_{\text{RR}}^{(i)}$, $\mathbf{s}_{\text{RF}}^{(i)}$, and $\mathbf{S}_{\text{RF}}^{(i)}$, where $i \in \{1, 2\}$, of both REMSs are continuous functions. Let $\mathbf{d} = d\hat{\mathbf{d}}$ be the Cartesian vector pointing from the center of the first REMS to the center of the second REMS, where d can be interpreted as the distance between the REMSs' and the unit vector $\hat{\mathbf{d}}$ characterizes their relative orientation to each other. Let $\ell^{(1)} \in [M^{(1)}]$ and $\ell^{(2)} \in [M^{(2)}]$. Then, as $d \rightarrow \infty$, the transmission coefficient from the $\ell^{(1)}$ th port of the first REMS to the $\ell^{(2)}$ th port of the second REMS is given by¹²*

$$\lim_{d \rightarrow \infty} S_{2_{\ell^{(2)}} 1_{\ell^{(1)}}} = \left(\mathbf{s}_{\text{RR}}^{(2)}(\ell^{(2)}; -\hat{\mathbf{d}}) \right)^T \mathbf{C} (\mathbf{I}_2 - \mathbf{M})^{-1} \mathbf{s}_{\text{RF}}^{(1)}(\ell^{(1)}; \hat{\mathbf{d}}), \quad (45)$$

where the matrices \mathbf{C} and \mathbf{M} are given by

$$\mathbf{M} \triangleq \mathbf{S}_{\text{RF}}^{(1)}(\hat{\mathbf{d}}; \hat{\mathbf{d}}) \mathbf{C} \mathbf{S}_{\text{RF}}^{(2)}(-\hat{\mathbf{d}}; -\hat{\mathbf{d}}) \mathbf{C} \quad (46)$$

$$\mathbf{C} \triangleq \frac{2\pi e^{-jk d}}{jk d} \begin{bmatrix} 1 & 0 \\ 0 & -1 \end{bmatrix}. \quad (47)$$

If the two REMSs in our example scenario are sufficiently far apart, then the desired transmission coefficients of the

¹²For convenience, we abuse the notation of the kernel function arguments in (45)–(47). Specifically, instead of using spherical altitude and azimuth coordinates, we represent directions with unit vectors (e.g., $\hat{\mathbf{d}}$).

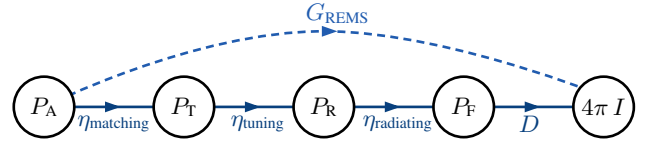


Figure 6. The relationship between various REMS power metrics is illustrated with solid lines. The REMS gain, which relates the radiation intensity to the available power from the power amplifiers, is represented by a dashed line. In general, the matching efficiency η_{match} , the tuning network efficiency η_{tuning} , the radiation efficiency $\eta_{\text{radiating}}$, and the directivity $D(\theta, \varphi)$ are all influenced by the voltage applied by the REMS power amplifiers and the configuration of the reconfigurable elements.

wireless channel can be calculated from the two REMSs' model parameters and the construction formula in (45).

E. Power and Gain Metrics

Besides the input-output relationships of a REMS and the wireless channels between multiple REMSs, one is often also interested in the total power output by the PAs, the radiated power of the REMS, or other related power metrics. We now define a range of potentially useful power metrics. We start with the following three interface-related power metrics.

Definition 5 (Interface-Related Power Metrics). *We define the tuning network accepted power as*

$$P_T \triangleq \Re\{\mathbf{v}_T^H \mathbf{i}_T\} = \|\mathbf{a}_T\|_2^2 - \|\mathbf{b}_T\|_2^2, \quad (48)$$

the radiating structure accepted power as

$$P_R \triangleq \Re\{\mathbf{v}_R^H \mathbf{i}_R\} = \|\mathbf{a}_R\|_2^2 - \|\mathbf{b}_R\|_2^2, \quad (49)$$

and the total far field radiated power as

$$P_F \triangleq P^{\nearrow} - P^{\searrow} = \|\mathbf{a}_F\|_{L^2}^2 - \|\mathbf{b}_F\|_{L^2}^2. \quad (50)$$

The right-hand side quantities in (48)–(50) are derived in Appendix A-F.

In contrast to these interface-related power metrics, which specify the actual power flowing into a subsystem, the next power metric specifies a potentially available power.

Definition 6 (Power Amplifiers Available Power). *For a fixed PA output voltage vector $\mathbf{v}_{\text{Tx}} \in \mathbb{C}^{N_{\text{Tx}}}$, we define the power amplifiers available power as*

$$P_A \triangleq \max_{\mathbf{S}_{\text{RR}}, \mathbf{S}_T} P_T \Big|_{\substack{\mathbf{v}_T = \mathbf{0} \\ \mathbf{i}_T = \mathbf{0} \\ \mathbf{v}_R = \mathbf{0} \\ \mathbf{b}_F = \mathbf{0}}} = \frac{1}{4} \mathbf{v}_{\text{Tx}}^H \Re\{\mathbf{Z}_{\text{Tx}}\}^{-1} \mathbf{v}_{\text{Tx}}, \quad (51)$$

where the vertical bar $|$ means “evaluated at.” The right-hand side quantity in (51) is derived in Appendix A-G.

The PAs' available power can now be used to define a new gain metric for REMSs acting as a transmitter.

Definition 7 (REMS Gain). *Given a REMS acting as a transmitter. Let $\mathbf{v}_{\text{Tx}} \in \mathbb{C}^{N_{\text{Tx}}}$ be the PA output voltage vector and $(\theta, \varphi) \in \Omega$ specify a direction. We define the REMS gain corresponding to \mathbf{v}_{Tx} and (θ, φ) as*

$$G_{\text{REMS}}(\mathbf{v}_{\text{Tx}}; \theta, \varphi) \triangleq \frac{1}{P_A} 4\pi I(\theta, \varphi) \Big|_{\substack{\mathbf{v}_T = \mathbf{0} \\ \mathbf{i}_T = \mathbf{0} \\ \mathbf{v}_R = \mathbf{0} \\ \mathbf{b}_F = \mathbf{0}}} \quad (52)$$

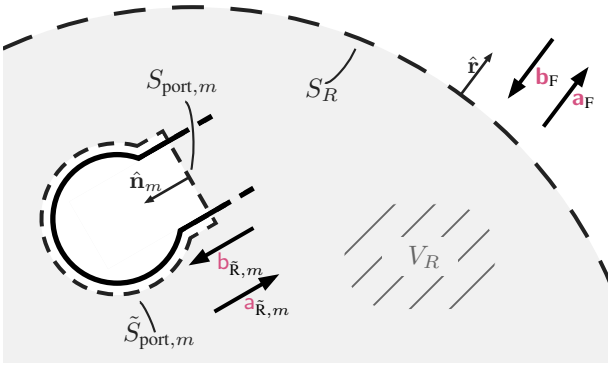


Figure 7. Qualitative sketch of the volume V_R and its surface ∂V_R . V_R is defined as the complement of a unit ball with radius R , minus the volume associated with the M (circuit-theoretic) ports that connect the REMS radiating part to the rest of the REMS. ∂V_R can be divided into S_R , $S_{\text{port},m}$, and $\tilde{S}_{\text{port},m}$ for $m \in [M]$. For each m , the surface $S_{\text{port},m}$ is the actual terminal surface of the m th port, while $\tilde{S}_{\text{port},m}$ denotes a surface inside the port's perfectly conducting shielding, so that $S_{\text{port},m} \cup \tilde{S}_{\text{port},m}$ forms a closed surface.

$$= 16\pi \frac{\|(\mathbf{G}_{\mathbf{v}_{\text{Tx}}}^{\text{aF}} \mathbf{v}_{\text{Tx}})(\theta, \varphi)\|_2^2}{\mathbf{v}_{\text{Tx}}^H \Re\{\mathbf{Z}_{\text{Tx}}\}^{-1} \mathbf{v}_{\text{Tx}}}. \quad (53)$$

The REMS gain G_{REMS} characterizes the combined effect of (i) the *REMS matching efficiency* $\eta_{\text{matching}} \triangleq P_{\text{T}}/P_{\text{A}}$, (ii) the *tuning network efficiency* $\eta_{\text{tuning}} \triangleq P_{\text{R}}/P_{\text{T}}$, (iii) the radiating structure's *radiation efficiency* $\eta_{\text{radiating}} \triangleq P_{\text{F}}/P_{\text{R}}$, and (iv) the radiation structure's *directivity* $D(\theta, \varphi) \triangleq (4\pi I(\theta, \varphi))/P_{\text{F}}$ as depicted in Figure 6; where $I(\theta, \varphi) = \|\mathbf{a}_{\text{F}}(\theta, \varphi)\|_2^2$ denotes the radiation intensity (cf. Remark 5).

Remark 6. The REMS gain G_{REMS} can be interpreted as the radiation intensity gain of the REMS relative to a reference system containing a single lossless, isotropically radiating antenna, whose feed is perfectly matched to the reference system PA's output stage, conditioned on that P_{A} of the REMS is equal to P_{A} of the reference system.

Remark 7. Analogous to the REMS gain G_{REMS} , one could also define gain metrics with respect to P_{T} and P_{R} . Moreover, for nonreciprocal REMS, it might be useful to distinguish between transmitting and receiving gain.

F. Reciprocity Relations for the Radiating Structure

In both purely academic and practical settings, it is often assumed that the wireless channel, including the radiating structure of all participating components, behaves in reciprocal manner. Whether a passive linear time-invariant wireless system behaves reciprocally or not is determined by the permittivity and permeability tensors describing the macroscopic material characteristics of the objects within the system. A sufficient condition for reciprocity is that all relevant materials are isotropic, meaning their properties do not change when tested in different directions. In this case, the permittivity and permeability tensors reduce to (position-dependent) scalar quantities. As a consequence of this, Lorenz reciprocity (cf. [65, Eq. 3.61]) holds. I.e., in a source-free reciprocal system, it holds that

$$\oint_{\partial V} \hat{\mathbf{n}}^T (\mathbf{E}_1 \times \mathbf{H}_2 - \mathbf{E}_2 \times \mathbf{H}_1) dS = 0 \text{ W}. \quad (54)$$

Here, V denotes an arbitrary volume within the source-free reciprocal system, dS denotes the area of the differential element on the surface of the volume V , \mathbf{E}_ℓ and \mathbf{H}_ℓ are the electric field and the magnetic field strength phasors, respectively, induced by one of two sources indexed by $\ell \in \{1, 2\}$, and $\hat{\mathbf{n}}$ is the outward pointing unit vector perpendicular to the surface ∂V .

In the following proposition, the impact of Lorentz reciprocity on the parameters of the radiation structure is explained. A proof of Proposition 3 can be found in Appendix A-C.

Proposition 3. Given a REMS for which Assumption 2 holds and whose M ports connecting the radiating part to the rest of the REMS support exactly one propagation mode¹³ each. For $R > 0$, we introduce the volume V_R as the complement of the unit ball with radius R (the REMS at its center) minus the volume occupied by the M ports, as sketched in Figure 7. Assume Lorentz reciprocity holds for the volume V_R as $R \rightarrow \infty$. Then, the parameters describing the REMS radiating structure display symmetrical properties. Specifically, it holds that

$$\mathbf{S}_{\text{RRR}} = \mathbf{S}_{\text{RRR}}^T \quad (55)$$

$$\mathbf{S}_{\text{RFF}} = \mathbf{S}_{\text{RFR}}, \quad (56)$$

and for all $(\theta, \varphi), (\theta', \varphi') \in \Omega$, it holds that

$$\mathbf{S}_{\text{RFF}}(\hat{\mathbf{r}}; \hat{\mathbf{r}}') = \mathbf{S}_{\text{RFF}}^T(\hat{\mathbf{r}}'; \hat{\mathbf{r}}), \quad (57)$$

where $\hat{\mathbf{r}}$, and $\hat{\mathbf{r}}'$ are the unit vectors corresponding to (θ, φ) and (θ', φ') , respectively.

Remark 8. It has been shown before that equations (55) and (57) are true for reciprocal systems. A proof of (57) can be found in [63, Eq. 7], for example. Furthermore, results similar to equation (56) can be found in the literature (e.g., in [48, Ch. II, Sec. 1.5]). However, to our knowledge, we are the first to prove the symmetry behavior of reciprocal systems in the form of (56), i.e., using the mathematical formalism based on spherical waves as introduced in Section II-B4.

G. Obtaining the Model Parameters

In order to obtain the model parameters describing the RF frontend and the tuning network, one can, for example, use simulations, measurements, or datasheets of the respective components. Which method is best suited depends on the application and is therefore not discussed further. Instead, we now explain how to extract the model parameters characterizing the radiating structure operator \mathbb{S}_{R} from a *single* full-wave EM simulation. A full-wave EM simulation can, for example, be conducted with Ansys HFSS [23]. We demonstrate how to obtain the model parameters for both reciprocal and non-reciprocal radiating structures.

As derived in Section II-B4, the operator \mathbb{S}_{R} from (17) is fully characterized by the matrix $\mathbf{S}_{\text{RRR}} \in \mathbb{C}^{M \times M}$ and the three kernels $\mathbf{s}_{\text{RFR}} : [M] \times \Omega \rightarrow \mathbb{C}^2$, $\mathbf{s}_{\text{RFF}} : [M] \times \Omega \rightarrow \mathbb{C}^2$, and $\mathbf{S}_{\text{RFF}} : \Omega \times \Omega \rightarrow \mathbb{C}^{2 \times 2}$. Unfortunately, the three kernels are, in general, infinite-dimensional and therefore cannot be represented by a computer. Consequently, we show how to

¹³With propagation mode, we refer to the specific way in which signals travel through a port.

obtain the matrix \mathbf{S}_{RRR} and the corresponding *sampled kernels*, which can be stored using a finite number of complex values.

Definition 8 (Sampled Kernels). *For a fixed finite subset $\tilde{\Omega} \subset \Omega$ we define the sampled kernels as the following functions:*

$$\mathbf{s}_{\text{RRR}}^{\text{sampled}} : [M] \times \tilde{\Omega} \rightarrow \mathbb{C}^2, (m; \theta, \varphi) \mapsto \mathbf{s}_{\text{RRR}}(m; \theta, \varphi) \quad (58)$$

$$\mathbf{s}_{\text{RRF}}^{\text{sampled}} : [M] \times \tilde{\Omega} \rightarrow \mathbb{C}^2, (m; \theta, \varphi) \mapsto \mathbf{s}_{\text{RRF}}(m; \theta, \varphi) \quad (59)$$

$$\mathbf{S}_{\text{RFF}}^{\text{sampled}} : \tilde{\Omega} \times \tilde{\Omega} \rightarrow \mathbb{C}^{2 \times 2}, (\theta, \varphi; \theta', \varphi') \mapsto \mathbf{S}_{\text{RFF}}(\theta, \varphi; \theta', \varphi'). \quad (60)$$

Remark 9. *Bucci and Franceschetti demonstrated in [66, Sec. 2-4] that the electric fields in the far-field region scattered by a spatially bounded object can be described by almost space-bandlimited functions. Motivated by this result, we assume that for each REMS, one can arbitrarily well represent the kernels \mathbf{s}_{RRR} , \mathbf{s}_{RRF} , and \mathbf{S}_{RFF} using the sampled kernels in Definition 8.*

The following paragraphs are organized such that each discusses how to obtain the model parameters associated with one of the four operators that constitute \mathbb{S}_{R} in (17).

1) *Inter-Element Coupling Operator \mathbb{S}_{RRR} :* Extracting \mathbf{S}_{RRR} through simulation software is straightforward and is therefore not discussed in detail. In general, M^2 complex values must be stored to fully characterize this operator. If the radiating structure behaves reciprocally, it follows from Proposition 3 that $\mathbf{S}_{\text{RRR}} = \mathbf{S}_{\text{RRR}}^{\text{T}}$. Consequently, in this case, roughly half of the complex values are sufficient to describe this operator.

2) *Transmitting Operator \mathbb{S}_{RRF} :* The sampled kernel $\mathbf{s}_{\text{RRF}}^{\text{sampled}}$ can be obtained by sequentially exciting each of the REMS's M ports, while terminating all other ports with the reference impedance R_0 . Consequently, when the m th port is excited with the circuit-theoretic power wave 1, it follows that $\mathbf{a}_{\tilde{\mathbf{R}}, m} = 1\sqrt{\tilde{W}}$, and for $n \neq m$ it holds that $\mathbf{a}_{\tilde{\mathbf{R}}, n} = 0\sqrt{\tilde{W}}$; where $\sqrt{\tilde{W}}$ is the respective physical unit¹⁴. By substituting $\mathbf{a}_{\tilde{\mathbf{R}}}$ into (18), it can be verified that for $(\theta, \varphi) \in \tilde{\Omega}$, $\mathbf{s}_{\text{RRF}}^{\text{sampled}}(m; \theta, \varphi)$ can be extracted from the outgoing far-field power wave pattern in the direction (θ, φ) . Storing the sampled kernel $\mathbf{s}_{\text{RRF}}^{\text{sampled}}$ necessitates storing $2M|\tilde{\Omega}|$ complex values.

3) *Receiving Operator \mathbb{S}_{RRF} :* For reciprocal systems, it holds that $\mathbf{s}_{\text{RRF}} = \mathbf{s}_{\text{RRR}}$ (see Proposition 3). Therefore, it is sufficient to extract only $\mathbf{s}_{\text{RRF}}^{\text{sampled}}$. For non-reciprocal systems, $\mathbf{s}_{\text{RRF}}^{\text{sampled}}$ must be extracted separately.

Extracting the sampled kernel $\mathbf{s}_{\text{RRF}}^{\text{sampled}}$ is a less straightforward task than obtaining \mathbf{S}_{RRR} and $\mathbf{s}_{\text{RRF}}^{\text{sampled}}$. The kernel $\mathbf{s}_{\text{RRF}}^{\text{sampled}}$ characterizes the REMS's response to incoming converging spherical waves, which currently are not typically simulated directly by simulation software. Instead, simulation software, such as Ansys HFSS, supports the simulation of scattering of an incoming plane wave with an electric field of the form

$$\mathbf{E}_{\text{p}}(r\hat{\mathbf{r}}) = \mathbf{q}e^{jk r\hat{\mathbf{r}}^{\text{T}}\hat{\mathbf{n}}_{\text{p}}}. \quad (61)$$

Here, the unit vector $\hat{\mathbf{n}}_{\text{p}}$ specifies the direction from which the wave is incoming and $\mathbf{q} \in \mathbb{C}^3$ specifies the amplitude and polarization of the plane wave. Fortunately, according to

¹⁴As explained in Section I-D in this paper we (only) explicitly write physical units when specifying numerical values.

Saxon [63, Eq. 16] and Nieto-Vesperinas [52, Eq. 5.45], in the far field of the scattering object, such a plane wave can be decomposed into an incoming and an outgoing spherical wave. Specifically, it holds that

$$\begin{aligned} \lim_{r \rightarrow \infty} \mathbf{E}_{\text{p}}(r\hat{\mathbf{r}}) &= \frac{2\pi}{jk} \mathbf{q} \delta(\hat{\mathbf{r}} - \hat{\mathbf{n}}_{\text{p}}) \frac{e^{+jkr}}{r} - \frac{2\pi}{jk} \mathbf{q} \delta(\hat{\mathbf{r}} + \hat{\mathbf{n}}_{\text{p}}) \frac{e^{-jkr}}{r}. \end{aligned} \quad (62)$$

From this decomposition and Definition 3 it follows that by generating a plane wave incoming from the direction indicated by the unit vector $\hat{\mathbf{n}}_{\text{p}}$, with RMS magnitude $\|\mathbf{E}_{\text{p}}\|_2 = \|\mathbf{q}\|_2$ and polarization specified by \mathbf{q} , one can determine the REMS's response to the incoming spherical wave characterized by $\mathbf{b}_{\text{F}} = \frac{2\pi}{jk\sqrt{Z_0}} \mathbf{q} \delta(\hat{\mathbf{r}} - \hat{\mathbf{n}}_{\text{p}})$. Consequently, it follows from (20) that for each $m \in [M]$, $(\theta, \varphi) \in \tilde{\Omega}$, the sampled kernel can be calculated as follows:

$$\mathbf{s}_{\text{RRF}}^{\text{sampled}}(m; \theta, \varphi) = \frac{jk\sqrt{Z_0}}{2\pi} \begin{bmatrix} \mathbf{b}_{\tilde{\mathbf{R}}, m} |_{\mathbf{q}=\hat{\theta}; \hat{\mathbf{n}}_{\text{p}}=\hat{\mathbf{r}}} \\ \mathbf{b}_{\tilde{\mathbf{R}}, m} |_{\mathbf{q}=\hat{\varphi}; \hat{\mathbf{n}}_{\text{p}}=\hat{\mathbf{r}}} \end{bmatrix}. \quad (63)$$

Here, $\mathbf{b}_{\tilde{\mathbf{R}}, m} |_{\mathbf{q}=\cdot; \hat{\mathbf{n}}_{\text{p}}=\hat{\mathbf{r}}}$ is the circuit-theoretic power wave as introduced in Definition 2 that is induced in port m by the plane wave incoming from (θ, φ) , with an (RMS) magnitude $\|\mathbf{E}_{\text{p}}\|_2 = 1$ V/m and the corresponding polarization.

Storing the sampled kernel $\mathbf{s}_{\text{RRF}}^{\text{sampled}}$ necessitates storing $2M|\tilde{\Omega}|$ complex values. Unfortunately, the sampled kernel cannot be directly inserted into (20). For this reason, we propose the following approximation formula, which utilizes the sampled kernel on $\mathbf{s}_{\text{RRF}}^{\text{sampled}}$ and can be implemented in a practical system:

$$\begin{aligned} [\mathbb{S}_{\text{RRF}} \mathbf{b}_{\text{F}}]_m &= \iint_{\tilde{\Omega}} \langle \mathbf{b}_{\text{F}}(\theta, \varphi), \bar{\mathbf{s}}_{\text{RRF}}(m; \theta, \varphi) \rangle_{\mathbb{C}^2} \sin(\theta) d(\theta, \varphi) \\ &\approx \sum_{(\theta, \varphi) \in \tilde{\Omega}} \langle \mathbf{b}_{\text{F}}(\theta, \varphi), \bar{\mathbf{s}}_{\text{RRF}}^{\text{sampled}}(m; \theta, \varphi) \rangle_{\mathbb{C}^2} A_{\tilde{\Omega}}(\theta, \varphi), \end{aligned} \quad (64)$$

$$\approx \sum_{(\theta, \varphi) \in \tilde{\Omega}} \langle \mathbf{b}_{\text{F}}(\theta, \varphi), \bar{\mathbf{s}}_{\text{RRF}}^{\text{sampled}}(m; \theta, \varphi) \rangle_{\mathbb{C}^2} A_{\tilde{\Omega}}(\theta, \varphi), \quad (65)$$

where $A_{\tilde{\Omega}}$ is a positive area weight function¹⁵ that only depends on the choice of $\tilde{\Omega}$. Note that the accuracy of the approximation in (65) depends on the kernel \mathbf{s}_{RRF} and the number of samples $|\tilde{\Omega}|$; see also the discussion in Section V on the limitations of our approach.

4) *Scattering Operator \mathbb{S}_{RFF} :* Similar to the receiving operator \mathbb{S}_{RRF} , one cannot directly insert the sampled kernel $\mathbf{s}_{\text{RFF}}^{\text{sampled}}$ into (21). Therefore, we propose the approximation

$$(\mathbb{S}_{\text{RFF}} \mathbf{b}_{\text{F}})(\theta, \varphi) = \iint_{\tilde{\Omega}} \mathbf{S}_{\text{RFF}}(\theta, \varphi; \theta', \varphi') \mathbf{b}_{\text{F}}(\theta', \varphi') d\Omega \quad (66)$$

$$\approx \sum_{(\theta', \varphi') \in \tilde{\Omega}} \mathbf{S}_{\text{RFF}}^{\text{sampled}}(\theta, \varphi; \theta', \varphi') \mathbf{b}_{\text{F}}(\theta', \varphi') A_{\tilde{\Omega}}(\theta', \varphi'). \quad (67)$$

Similar as in (65), the accuracy of the approximation in (67) depends on the kernel \mathbf{S}_{RFF} and the number of samples $|\tilde{\Omega}|$.

As with the receiving operator \mathbb{S}_{RRF} , when attempting to obtain $\mathbf{S}_{\text{RFF}}^{\text{sampled}}$ from simulation software, one encounters

¹⁵Such a choice of $A_{\tilde{\Omega}} > 0$ can, for example, be constructed using a Voronoi diagram on the unit sphere.

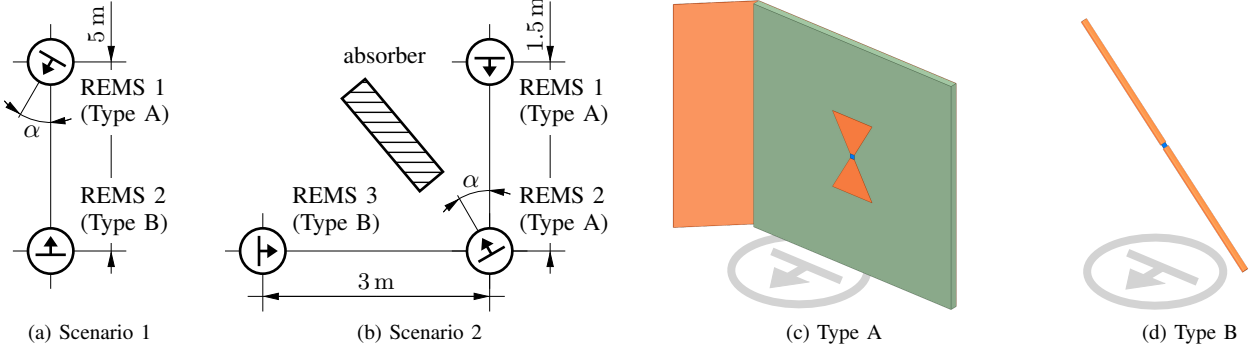


Figure 8. The setup of the two scenarios are illustrated in (a) and (b). All elements lie in the xy -plane ($\theta = 90^\circ$). Moreover, the (circuit-theoretic) ports of all REMSs are terminated with the reference impedance of $R_0 = 50 \Omega$. The structures of the two REMS types used in the scenarios are illustrated in (c) and (d). The colors represent the following: orange for copper, green for Rogers 3203, and blue for the lumped ports. The two REMS types are not to scale relative to each other; subfigures (c) and (d) contain screenshots taken from Ansys HFSS.

the problem that generating incoming converging spherical waves is typically not directly supported by full-wave EM simulation software. By applying the same approach proposed in Section II-G3, the total electric far field can be expressed as

$$\lim_{r \rightarrow \infty} \mathbf{E}(r\hat{\mathbf{r}}) = \mathbf{q}e^{+jkr\hat{\mathbf{r}}^T\hat{\mathbf{n}}_p} + \mathbf{s}_q(\hat{\mathbf{r}}, \hat{\mathbf{n}}_p) \frac{e^{-jkr}}{r} \quad (68)$$

$$= \frac{2\pi}{jk} \mathbf{q} \delta(\hat{\mathbf{r}} - \hat{\mathbf{n}}_p) \frac{e^{+jkr}}{r} + \left(\mathbf{s}_q(\hat{\mathbf{r}}, \hat{\mathbf{n}}_p) - \frac{2\pi}{jk} \mathbf{q} \delta(\hat{\mathbf{r}} + \hat{\mathbf{n}}_p) \right) \frac{e^{-jkr}}{r}, \quad (69)$$

where $\mathbf{s}_q(\hat{\mathbf{r}}, \hat{\mathbf{n}}_p)$ is the complex amplitude characterizing the scattered electric field traveling in the direction $\hat{\mathbf{r}}$, when the REMS is excited by a plane wave incoming from $\hat{\mathbf{n}}_p$ with polarization \mathbf{q} and an (RMS) electric field magnitude of $\|\mathbf{E}\|_2 = 1 \text{ V/m}$. Continuing from (69), it was deduced by Saxon how the kernel \mathbf{S}_{RFF} can be constructed explicitly. We adapt Saxon's construction formula [63, Eq. 21] to our framework to obtain

$$\mathbf{S}_{\text{RFF}}^{\text{sampled}}(\theta, \varphi; \theta', \varphi') = - \begin{bmatrix} 1 & 0 \\ 0 & -1 \end{bmatrix} \frac{1}{A_{\tilde{\Omega}}(-\theta', -\varphi')} \delta_{\theta, -\theta'} \delta_{\varphi, -\varphi'} + \frac{jk}{2\pi} \underbrace{\begin{bmatrix} [\mathbf{s}_{\hat{\theta}'}(\theta, \varphi; \theta', \varphi')]_{\hat{\theta}} & [\mathbf{s}_{\hat{\varphi}'}(\theta, \varphi; \theta', \varphi')]_{\hat{\theta}} \\ [\mathbf{s}_{\hat{\theta}'}(\theta, \varphi; \theta', \varphi')]_{\hat{\varphi}} & [\mathbf{s}_{\hat{\varphi}'}(\theta, \varphi; \theta', \varphi')]_{\hat{\varphi}} \end{bmatrix}}_{\triangleq \tilde{\mathbf{S}}_{\text{RFF}}^{\text{sampled}}}, \quad (70)$$

where the appearance of the Pauli matrix is a consequence of the spherical coordinate system we use in Definition 3; and where we introduced the *reduced sampled kernel of the scattering operator* $\tilde{\mathbf{S}}_{\text{RFF}}^{\text{sampled}}$. Inserting (70) into (67) leads to

$$(\mathbf{S}_{\text{RFF}} \mathbf{b}_F)(\theta, \varphi) \approx - \begin{bmatrix} 1 & 0 \\ 0 & -1 \end{bmatrix} \mathbf{b}_F(\pi - \theta, \pi + \varphi) + \sum_{(\theta', \varphi') \in \tilde{\Omega}} \tilde{\mathbf{S}}_{\text{RFF}}^{\text{sampled}}(\theta, \varphi; \theta', \varphi') \mathbf{b}_F(\theta', \varphi') A_{\tilde{\Omega}}(\theta', \varphi'). \quad (71)$$

It is evident that, in a practical implementation, it is sufficient to store the *reduced* sampled kernel of the scattering operator $\tilde{\mathbf{S}}_{\text{RFF}}^{\text{sampled}}$. Storing $\tilde{\mathbf{S}}_{\text{RFF}}^{\text{sampled}}$ instead of $\mathbf{S}_{\text{RFF}}^{\text{sampled}}$ offers numerical advantages, as the first term in (70) includes $(A_{\tilde{\Omega}}(\cdot, \cdot))^{-1}$, whose magnitude tends to grow linearly with the number of samples $|\tilde{\Omega}|$.

III. EXPERIMENTAL VALIDATION

We now use numerical experiments to validate the proposed REMS-far-field-interaction formalism from Section II-B4 and the proposed method for obtaining the radiating structure parameters from Section II-G. In particular, we compare predictions made using our REMS far-field interaction formalism with Ansys HFSS simulation results in two scenarios.

A. Scenario 1

In the first scenario, there are two REMSs placed in empty space, as illustrated in Figure 8a. The REMS types involved are shown in Figure 8c and Figure 8d: a patch antenna (type A) and a half-wave dipole antenna (type B), each with one antenna port ($M = 1$). The wireless channel between the two REMSs can be manipulated by varying the rotation angle α of REMS 1. We analyze the system at a frequency of 5.4 GHz and compare the following two methods.

For the *proposed* method, we first use the approach described in Section II-G to obtain the parameters characterizing the radiating structures of both REMS types, relying on a single full-wave EM simulation for each REMS type. Second, for each rotation angle α , we utilize Proposition 2 to calculate the transmission coefficient (cf. Definition 4) from REMS 1 to REMS 2 ($S_{21,1}$). For the *conventional* method, we use Ansys HFSS to simulate the complete scenario, including both REMSs, for each rotation angle α to obtain $S_{21,1}$.

Figure 9 shows the results of the proposed and the conventional method. The two methods agree well over the analyzed range of α . We attribute the small deviations between the two methods to (i) the finite separation distance between the two REMSs in this scenario, whereas in Proposition 2 we assume that the separation distance approaches infinity, and (ii) numerical inaccuracies in the *conventional* method. We refer to Section III-C for a discussion on the numerical stability and required computational resources of the proposed and conventional methods.

The good agreement between the proposed and conventional methods validates (i) the proposed REMS-far-field-interaction formalism and (ii) the proposed method for obtaining the model parameters of the REMS radiating structure. Specifically, the

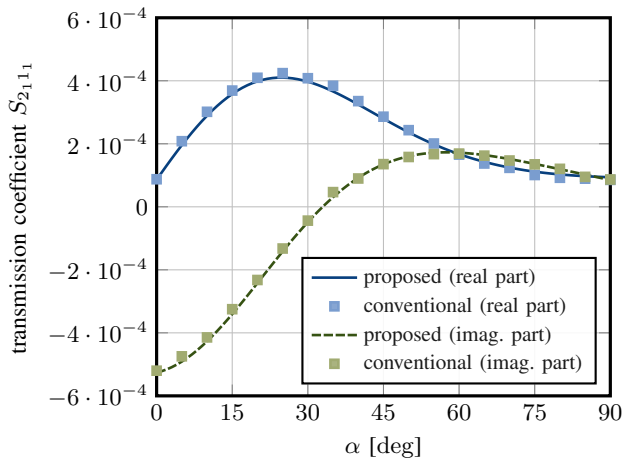


Figure 9. Results for Scenario 1. The transmission coefficients obtained by (i) the proposed method and (ii) the conventional method are plotted for various angles α . The results of the two methods agree well over the entire analyzed range of α .

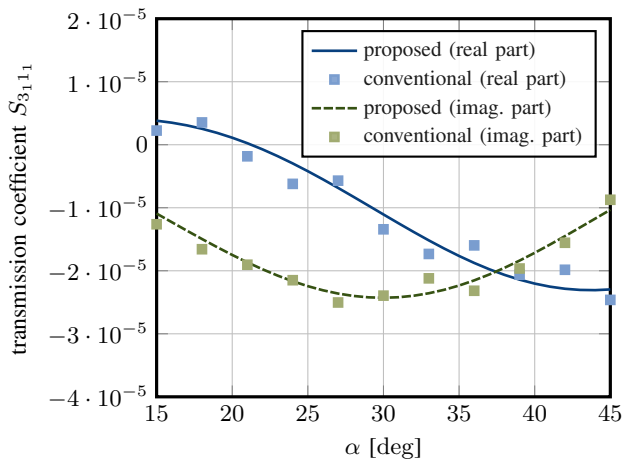


Figure 10. Results for Scenario 2. The transmission coefficients obtained by (i) the proposed method and (ii) the conventional method are plotted for various angles α . The results of the two methods generally agree. However, the results from the conventional method exhibit noise, which we attribute to numerical stability issues.

results of Scenario 1 validate our *modeling* of the transmitting operator \mathbb{S}_{RFR} in (18), and the receiving operator \mathbb{S}_{RRF} in (20) as well as the *extraction* of the respective kernels \mathbf{s}_{RFR} and \mathbf{s}_{RRF} . Because we presume that the influence of the scattering operator \mathbb{S}_{RFF} on the transmission coefficient is negligibly small in this scenario, additional experiments, which are shown next, are required to validate the respective modeling approach in (21) and the method for obtaining the kernel \mathbf{S}_{RFF} in (70).

B. Scenario 2

In this scenario, there are three REMSs placed in empty space, as illustrated in Figure 8b. We use the same REMS types as in Scenario 1 (see Figure 8c and Figure 8d). The wireless channel between the three REMSs can be manipulated

by varying the rotation angle α of REMS 2. The absorber¹⁶ between REMS 1 and REMS 3 ensures that the scattering operator $\mathbb{S}_{\text{RFF}}^{(A)}$ of REMS 2 significantly impacts the result. Again, we analyze the system at a frequency of 5.4 GHz.

We mainly follow the same methodology used in Scenario 1 to determine the transmission coefficient $S_{3,1,1}$ (cf. Definition 4) from REMS 1 to REMS 3 using both the *proposed* and the *conventional* methods. In contrast to Scenario 1, for the proposed method, we now use the approximation

$$S_{3,1,1} \approx \left(\mathbf{s}_{\text{RFR}}^{(B)}(1; 90^\circ, 0^\circ) \right)^\top \mathbf{C}_{23} \cdot \mathbf{S}_{\text{RFF}}^{(A)}(90^\circ, 90^\circ - \alpha; 90^\circ, -\alpha) \mathbf{C}_{12} \mathbf{s}_{\text{RFR}}^{(A)}(1; 90^\circ, 0^\circ) \quad (72)$$

instead of Proposition 2 to calculate the transmission coefficient¹⁷, where the matrices \mathbf{C}_{12} and \mathbf{C}_{23} are defined as follows:

$$\mathbf{C}_{12} \triangleq \frac{2\pi}{jk} \frac{e^{-jk \cdot 1.5 \text{ m}}}{1.5 \text{ m}} \begin{bmatrix} 1 & 0 \\ 0 & -1 \end{bmatrix} \quad (73)$$

$$\mathbf{C}_{23} \triangleq \frac{2\pi}{jk} \frac{e^{-jk \cdot 3 \text{ m}}}{3 \text{ m}} \begin{bmatrix} 1 & 0 \\ 0 & -1 \end{bmatrix}. \quad (74)$$

Figure 10 shows the results of the proposed and conventional method. The two methods generally agree over the analyzed range of α , but the relative deviations between them are more pronounced than in Scenario 1. We attribute these deviations primarily to errors resulting from numerical inaccuracies of the *conventional* method (see Section III-C).

Together with the results from Scenario 1, the agreement between the methods shown in Figure 10 validates the REMS scattering operator approach in (21) and the method for obtaining the kernel \mathbf{S}_{RFF} . Thus, we have validated that our proposed modeling approach for the transmitting operators \mathbb{S}_{RFR} , the receiving operators \mathbb{S}_{RRF} , and the scattering operators \mathbb{S}_{RFF} is correct. Furthermore, we have validated that the proposed method for obtaining the respective kernels for these three operators is also correct.

C. Numerical Stability and Computational Resources

The transmission coefficients obtained using the conventional method exhibit noise, as can be seen particularly in Figure 10.¹⁸ We observed that the variance of this noise-like behavior reduced when investing more computational resources, i.e., additional CPU time and memory. As a comparison, to generate Figure 9 and Figure 10, for the conventional method, we invested roughly 120 CPU-hours to obtain 30 transmission coefficients, while our proposed method required only about 0.5 CPU-hours to generate 132 transmission coefficients.¹⁹ We have the following explanations for these observations.

¹⁶For numerical stability reasons, we did not include an absorber in the Ansys HFSS simulation of the conventional method. Instead, we conducted an additional simulation without REMS 2 to isolate the contribution of the direct path between REMS 1 and REMS 3 to the transmission coefficient $S_{3,1,1}$. We then subtracted this contribution from the main simulation result.

¹⁷Equation (72) can be derived by adapting the proof of Proposition 2 to Scenario 2 and applying the unilateral approximation from [38, Sec. II-F].

¹⁸In Figure 10, the y-axis scale is 20 times smaller than that of Figure 9.

¹⁹We did not optimize the simulation settings for either method to achieve best performance. Therefore, the CPU hours provided here only serve as a rough comparison of the computational effort.

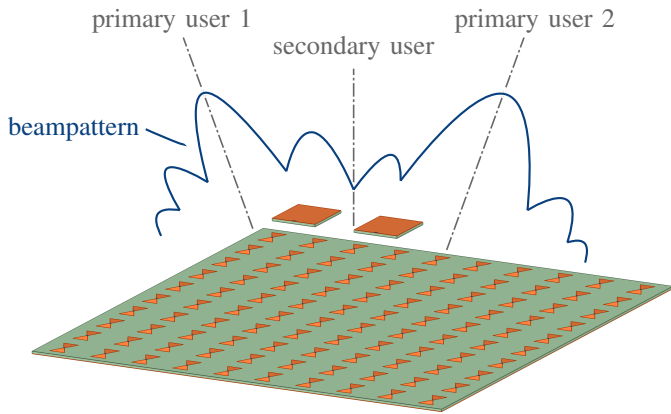


Figure 11. Conceptual sketch of the case study. It shows the reconfigurable reflectarray (RRA) used in this study (screenshot from Ansys HFSS). The RRA consists of two downward-facing, actively fed patch antennas and 100 passive configurable reflective elements on the main substrate, spaced $\lambda/2$ apart (at an analysis frequency of 5.4 GHz). The RRA steers its beam pattern toward two primary users while minimizing power toward a secondary user.

For the conventional method, we simulate the complete scenario at once. In doing so, the simulation software must describe both the EM fields in the transmitting REMS and the much weaker EM fields around the receiving REMS. We presume that the need to handle both strong and comparably extremely weak signals makes the conventional method susceptible to numerical issues. Consequently, extensive computational resources are required for the conventional method to accurately predict the transmission coefficients. In contrast, our proposed method, where the two REMS types are simulated separately, is significantly more numerically stable. Moreover, the conventional method requires a completely new simulation for every physical change in the system (e.g., for every different angle α). In contrast, our proposed method requires only one Ansys HFSS simulation for each REMS type to obtain the radiating structure parameters (cf. Section II-G).

As a consequence, the proposed method can predict transmission coefficients orders of magnitude faster than the conventional method, while producing more accurate results. Because of this behavior, in both scenarios, we generated results for many more angles α using the proposed method than with the conventional method. Consequently, in Figure 9 and Figure 10, we illustrate the results of the proposed method with a continuous curve and those of the conventional method with discrete samples.

IV. CASE STUDY: PHYSICALLY-ACCURATE BEAM- AND NULLFORMING WITH A RECONFIGURABLE REFLECTARRAY

In order to demonstrate the efficiency and the physical consistency of the model proposed in Section II, we now provide a case study that focuses on a reconfigurable reflectarray (RRA) as depicted in Figure 11.²⁰ This RRA is a hybrid analog-digital beamforming system, and we analyze its behavior when it acts as a transmitter. The goal of the RRA is to steer its transmit beams towards $U \leq N$ primary users (e.g., communication

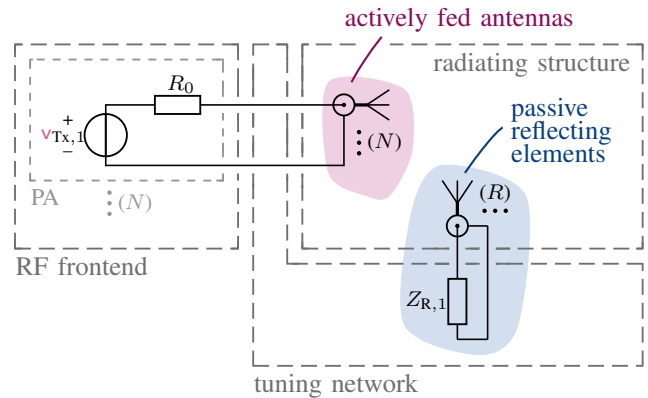


Figure 12. Basic structure of a simple reconfigurable reflectarray (RRA) that acts as a transmitter. The RRA consists of N actively fed antennas whose signals are reflected by R passive reflecting elements. The behavior of the reflector elements can be reconfigured by changing the value of the impedances $Z_{R,1}, \dots, Z_{R,R}$. The dashed boxes divide the RRA into the three submodels illustrated in Figure 2.

partners) while minimizing the power directed towards $I \in \mathbb{Z}_{\geq 0}$ secondary users (e.g., other receiving devices that are not part of the communication system). This RRA uses the basic structure illustrated in Figure 12, with $N = 2$ actively fed patch antennas and a large number ($R = 100$) of passive and configurable reflective elements arranged as a 10×10 rectangular array. For $r \in [R]$, the r th passive reflective element features a tunable impedance $Z_{R,r}$.

A. Proposed Algorithm

To perform simultaneous beam- and null-forming, we propose an efficient and physics-aware algorithm that jointly optimizes the configuration of the RRA's reconfigurable elements and the digital precoding matrix. We represent the values of the R impedances in the tuning network with the tuple $\mathbf{Z}_R \triangleq (Z_{R,1}, \dots, Z_{R,R})$. Furthermore, we denote the finite set of potential impedance values that can be chosen for each reconfigurable impedance as $Z_R \subset \{c \in \mathbb{C} \mid \Re\{c\} \geq 0\}$ ²¹; i.e., it holds that $\mathbf{Z}_R \in Z_R^R$. For each primary user indexed by $u \in [U]$, let $s_u \in \mathbb{C}$ be the symbol to be transmitted to primary user u , and define the symbol vector as $\mathbf{s} \triangleq [s_1, \dots, s_U]^T$. Let $\mathbf{T} \in \mathbb{C}^{N \times U}$ denote the precoding matrix, such that $\mathbf{v}_{Tx} \triangleq \mathbf{T}\mathbf{s}$ is the precoded PA output voltage vector.

To steer the RRA's beams towards the primary users and minimize the energy towards the secondary users, the algorithm *jointly optimizes* the analog reconfigurable impedances \mathbf{Z}_R (equal to analog beam- and null-forming) and the precoding matrix \mathbf{T} (equal to digital beam- and null-forming). We assume that the algorithm is provided with the directions of all primary users $\{(\theta_{U,1}, \varphi_{U,1}), \dots, (\theta_{U,U}, \varphi_{U,U})\}$ and all secondary users $\{(\theta_{I,1}, \varphi_{I,1}), \dots, (\theta_{I,I}, \varphi_{I,I})\}$.

²⁰An Ansys HFSS project file containing the modeled RRA can be downloaded from <https://github.com/IIP-Group/RRA-case-study>.

1) *Underlying Optimization Problem:* For $u \in [U]$, let \mathbf{e}_u be the u th column of the identity matrix \mathbf{I}_U . We now introduce the following quasi-power²² terms:

$$\tilde{P}_{\text{signal}}(\mathbf{Z}_R, \mathbf{T}) \triangleq \min_{u \in [U]} G_{\text{REMS}}(\mathbf{T}\mathbf{e}_u; \theta_{U,u}, \varphi_{U,u}) \quad (75)$$

$$\tilde{P}_{\text{interf.}}(\mathbf{Z}_R, \mathbf{T}) \triangleq \max_{\substack{u, u' \in [U]: \\ u' \neq u}} G_{\text{REMS}}(\mathbf{T}\mathbf{e}_{u'}; \theta_{U,u}, \varphi_{U,u}) \quad (76)$$

$$\tilde{P}_{\text{second.}}(\mathbf{Z}_R, \mathbf{T}) \triangleq \max_{u \in [U], \iota \in [I]} G_{\text{REMS}}(\mathbf{T}\mathbf{e}_u; \theta_{I,\iota}, \varphi_{I,\iota}). \quad (77)$$

Here, G_{REMS} is the REMS gain (see Definition 7) of the RRA when the impedance values \mathbf{Z}_R in the argument of the quasi-power terms are used for the reconfigurable impedances²³. The optimization problem underlying our algorithm can now be stated as follows:

$$\underset{\substack{\mathbf{Z}_R \in \mathcal{Z}_R^R \\ \mathbf{T} \in \mathbb{C}^{N \times U}}}{\text{maximize}} \frac{\tilde{P}_{\text{signal}}(\mathbf{Z}_R, \mathbf{T})}{\tilde{P}_{\text{interf.}}(\mathbf{Z}_R, \mathbf{T}) + \tilde{P}_{\text{second.}}(\mathbf{Z}_R, \mathbf{T})}. \quad (78)$$

Informally, (75)–(78) can be interpreted as the algorithm jointly optimizing the impedances \mathbf{Z}_R and the precoding matrix \mathbf{T} to minimize the ratio of the minimum received signal power at the U primary users to the sum of the maximal interference power at the U primary users and the maximal power radiated in the direction of the I secondary users.

2) *Algorithm Overview:* The optimization problem in (78) can be reformulated as

$$\underset{\substack{\mathbf{Z}_R \in \mathcal{Z}_R^R \\ \mathbf{T} \in \mathbb{C}^{N \times U}}}{\text{maximize}} \max_{\mathbf{T} \in \mathbb{C}^{N \times U}} \frac{\tilde{P}_{\text{signal}}(\mathbf{Z}_R, \mathbf{T})}{\tilde{P}_{\text{interf.}}(\mathbf{Z}_R, \mathbf{T}) + \tilde{P}_{\text{second.}}(\mathbf{Z}_R, \mathbf{T})}. \quad (79)$$

Our proposed algorithm heuristically addresses the inner maximization problem in (79) by first approximating the wireless channel matrix between the N PAs of the RRA and the U primary users. Second, the algorithm applies this channel matrix and the zero-forcing precoding scheme (see [67, Sec. 4]) to compute the precoding matrix \mathbf{T} .

Since the set \mathcal{Z}_R^R is finite, the outer maximization problem in (79) is of combinatorial nature. As the number of choices for \mathbf{Z}_R grows exponentially with R , an exhaustive search is infeasible. We, therefore, propose a heuristic optimization approach based on coordinate ascent [68, Sec. 2.3.1], which is computationally efficient. Specifically, the algorithm operates iteratively, optimizing the reconfigurable impedance tuple \mathbf{Z}_R . During each iteration, all but one entry in \mathbf{Z}_R are held fixed. For the non-fixed entry, the algorithm tests all values from \mathcal{Z}_R to maximize an objective function, which we define below.

3) *Algorithm Details:* The proposed approach is detailed in Algorithm 1. The main iteration loop (see lines 4–18) is executed I_{max} times. In each iteration of the main loop, a new pseudo-random permutation (denoted by the tuple $\tilde{\mathbf{R}}$) of the elements in the set $[R]$ is generated (see line 5). Based on this permutation, the algorithm iterates over all R reconfigurable impedances (see lines 6–17). During each iteration of this inner loop, all reconfigurable impedances are fixed except one, which is indexed by r .

²²We use “quasi-power” because one can informally interpret the in (75)–(77) defined terms as power metrics, even though they do not represent a physical power.

²³The effect of the argument \mathbf{Z}_R is not shown explicitly to simplify notation.

Algorithm 1 Physically-Accurate Beam- and Nullforming

Input: $R_0 \in \mathbb{R}_{>0}$, $N \in \mathbb{N}$, $R \in \mathbb{N}$, $\mathcal{Z}_R \subset \{c \in \mathbb{C} \mid \Re\{c\} \geq 0\}$,
 $\mathcal{Z}_R^{\text{init}} \in \mathcal{Z}_R$, $I_{\text{max}} \in \mathbb{N}$, $(\sigma_i)_{i \in [I_{\text{max}}]}$, $\hat{\mathbf{q}}_{\text{co}} : \Omega \rightarrow \mathbb{C}^2$,
 $U \leq N$, $(\theta_{U,1}, \varphi_{U,1}), \dots, (\theta_{U,U}, \varphi_{U,U}) \in \Omega$,
 $I \in \mathbb{Z}_{\geq 0}$, $(\theta_{I,1}, \varphi_{I,1}), \dots, (\theta_{I,I}, \varphi_{I,I}) \in \Omega$

Output: \mathbf{Z}_R, \mathbf{T}

Initialization:

- 1: $\mathbf{Z}_R^{\text{best}} \triangleq (Z_{R,1}^{\text{best}}, \dots, Z_{R,R}^{\text{best}}) \leftarrow (Z_{R,1}^{\text{init}}, \dots, Z_{R,R}^{\text{init}})$
 - 2: $\mathbf{T}^{\text{best}} \leftarrow [\mathbf{I}_N \quad \mathbf{0}_{N, N-U}]^T$
 - 3: $f^{\text{best}} \leftarrow 0$
-

Iterative Process:

- 4: **for** $i = 1$ to I_{max} **do**
 - 5: $\tilde{\mathbf{R}} \leftarrow$ random permutation of the elements of $[R]$
 - 6: **for** r in $\tilde{\mathbf{R}}$ **do**
 - 7: **for** z in \mathcal{Z}_R **do**
 - 8: $\mathbf{Z}_R^{\text{eval}} \leftarrow (\dots; Z_{R,r-1}^{\text{best}}, z, Z_{R,r+1}^{\text{best}}, \dots)$
 - 9: $\mathbf{H}_U \leftarrow \mathbf{H}_{\text{co}}(\mathbf{Z}_R^{\text{eval}})$
 - 10: $\mathbf{T}^{\text{ZF}} \leftarrow \mathbf{H}_U^H (\mathbf{H}_U \mathbf{H}_U^H)^{-1}$
 - 11: **if** $f(\mathbf{Z}_R^{\text{eval}}, \sigma_i; \mathbf{T}^{\text{ZF}}) > f^{\text{best}}$ **then**
 - 12: $\mathbf{Z}_R^{\text{best}} \leftarrow \mathbf{Z}_R^{\text{eval}}$
 - 13: $\mathbf{T}^{\text{best}} \leftarrow \mathbf{T}^{\text{ZF}}$
 - 14: $f^{\text{best}} \leftarrow f(\mathbf{Z}_R^{\text{best}}, \sigma_i; \mathbf{T}^{\text{best}})$
 - 15: **end if**
 - 16: **end for**
 - 17: **end for**
 - 18: **end for**
 - 19: **return** $\mathbf{Z}_R^{\text{best}}, \mathbf{T}^{\text{best}}$
-

With an additional innermost loop, the best possible value for the non-fixed impedance is searched over the set \mathcal{Z}_R (see lines 7–16). Specifically, the reconfigurable impedance tuple $\mathbf{Z}_R^{\text{eval}}$ used for evaluation in the corresponding coordinate ascent step is first constructed on line 8. Then, the channel to the U primary users is calculated using the function \mathbf{H}_{co} on line 9. The function \mathbf{H}_{co} is defined as follows:

$$\mathbf{H}_{\text{co}}(\mathbf{Z}_R) \triangleq \begin{bmatrix} \hat{\mathbf{q}}_{\text{co}}^T(\theta_{U,1}, \varphi_{U,1}) \left(\mathbb{G}_{\mathbf{v}_{\text{Tx}}}^{\text{aF}}(\theta_{U,1}, \varphi_{U,1}) \right) \\ \vdots \\ \hat{\mathbf{q}}_{\text{co}}^T(\theta_{U,U}, \varphi_{U,U}) \left(\mathbb{G}_{\mathbf{v}_{\text{Tx}}}^{\text{aF}}(\theta_{U,U}, \varphi_{U,U}) \right) \end{bmatrix}. \quad (80)$$

Here, the matrix $(\mathbb{G}_{\mathbf{v}_{\text{Tx}}}^{\text{aF}}(\theta, \varphi))$ corresponds to the linear map defined by $\mathbb{C}^{N_{\text{Tx}}} \rightarrow \mathbb{C}^2$, $\mathbf{v} \mapsto (\mathbb{G}_{\mathbf{v}_{\text{Tx}}} \mathbf{v})(\theta, \phi)$ and $\hat{\mathbf{q}}_{\text{co}} : \Omega \rightarrow \mathbb{C}^2$ is an RRA-dependent function that should approximate the polarization of the transmitted electromagnetic waves as accurately as possible.²⁴

Finally, a potential precoding matrix \mathbf{T}^{ZF} , which is used for evaluation in the current coordinate ascent step, is calculated

²⁴Informally, if all radiating components (e.g., antennas or reflective elements) of the REMS have the same polarization, then $\hat{\mathbf{q}}_{\text{co}}$ should approximate the co-polarization of these radiating components in the far field of the REMS.

using zero forcing (see, e.g., [67, Sec. 4]) on line 10. Note that, for the calculation of the precoding matrix, only the channels to the primary users, but not to the secondary users, are considered. The coordinate ascent objective function is given by

$$f(\mathbf{Z}_R, \sigma; \mathbf{T}^{\text{ZF}}) \triangleq \frac{\tilde{P}_{\text{signal}}(\mathbf{Z}_R, \mathbf{T}^{\text{ZF}})}{\tilde{P}_{\text{interf.}}(\mathbf{Z}_R, \mathbf{T}^{\text{ZF}}) + \tilde{P}_{\text{second.}}(\mathbf{Z}_R, \mathbf{T}^{\text{ZF}}) + \sigma}, \quad (81)$$

where $\sigma \geq 0$ is a regularization parameter, which weights²⁵ the contribution of the quasi-power terms $\tilde{P}_{\text{signal}}$, $\tilde{P}_{\text{interf.}}$, and $\tilde{P}_{\text{second.}}$. On line 11, the algorithm checks whether the objective function, using $\mathbf{Z}_R^{\text{eval}}$, is strictly greater than f_{best} and updates the respective parameters accordingly on lines 12–14.

B. Numerical Simulations

We now show the results of our beam- and nullforming algorithm for the RRA depicted in Figure 11. To this end, we set the reference impedance to $R_0 = 50 \Omega$. We assume that the reconfigurable impedances are implemented using varactors. Based on the specifications of the MCE Metelics MGV-100-21 varactor [69], we assume a constant resistance of 1.2Ω and an adjustable reactance within the range of -196Ω to -14Ω at the operating frequency of 5.4 GHz. The set of available impedance values, \mathbf{Z}_R , was constructed by sampling 32 uniformly spaced values from this range. Furthermore, we set the number of main iterations of our algorithm to $I_{\text{max}} = 10$ and set the (iteration dependent) regularization parameter to $\sigma_i = 20(0.5)^i$ for $i \in [I_{\text{max}}]$. Motivated by the observation that both the two actively fed antennas and the passive reflecting elements are aligned along the x-axis (in Cartesian coordinates), we provide the algorithm with the polarization estimation function $\hat{\mathbf{q}}_{\text{co}}(\theta, \phi) = [\cos(\phi), -\sin(\phi)]^T$, which corresponds to the co-polarization of a perfectly linearly polarized antenna along the x-axis. To simplify visualization of the simulation results provided next, we introduce negative altitude angles ($\theta < 0^\circ$). Specifically, for $\theta \in [-180^\circ, 0^\circ]$ and $\varphi \in \mathbb{R}$, the direction (θ, φ) refers to $(-\theta, \varphi + 180^\circ)$.

Figure 13 shows the results of the first simulation. Here, one primary user was placed at $\theta_{U,1} = 30^\circ$ and $\varphi_{U,1} = 0^\circ$ and one secondary user at $\theta_{I,1} = 15^\circ$ and $\varphi_{I,1} = 0^\circ$. The algorithm was then run twice: once ignoring the secondary user and once considering both users. In both cases, our algorithm achieves a gain of more than 12 dB in the direction of the primary user. That is, our algorithm is able to suppress the transmitted radiation intensity in the direction of the secondary user while still upholding the REMS gain in the direction of the primary user.

Figure 14 shows the results of the second simulation, where an additional primary user is placed at $\theta_{U,2} = 0^\circ$ and $\varphi_{U,2} = 0^\circ$. Since there are now two primary users, we show the REMS gain for the case where $\mathbf{v}_{\text{Tx}} = \mathbf{T}\mathbf{e}_1$ to visualize the beam when a signal is sent to the first primary user. Additionally, we show the REMS gain for the case where $\mathbf{v}_{\text{Tx}} = \mathbf{T}\mathbf{e}_2$ to visualize the beam when a signal is sent

²⁵A positive regularization parameter $\sigma > 0$ improves numerical stability.

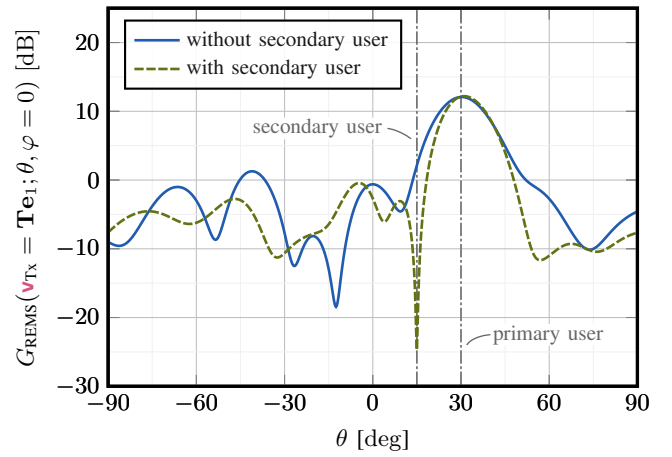


Figure 13. REMS gain G_{REMS} in the $\varphi = 0^\circ$ slice that is achieved by applying Algorithm 1 to the first simulation scenario. The algorithm is able to suppress the transmitted radiation intensity in the direction of the secondary user while upholding a REMS gain of more than 12 dB into the direction of the primary user. Both traces were calculated using (53).

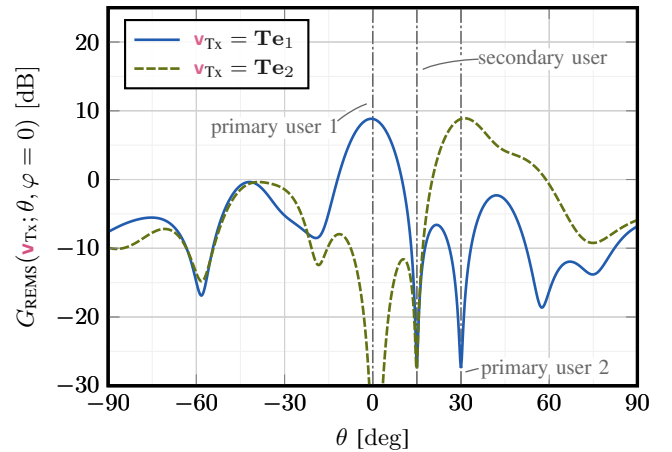


Figure 14. REMS gain G_{REMS} in the $\varphi = 0^\circ$ slice that is achieved by applying Algorithm 1 to the second simulation scenario. The blue curve ($\mathbf{v}_{\text{Tx}} = \mathbf{T}\mathbf{e}_1$) at $\theta = 0^\circ$ and the green curve ($\mathbf{v}_{\text{Tx}} = \mathbf{T}\mathbf{e}_2$) at $\theta = 30^\circ$ show the REMS gain in the direction of both primary users is slightly more than 8.5 dB. Moreover, we see from both curves at $\theta \in \{0^\circ, 15^\circ, 30^\circ\}$ that (i) the signals intended for the primary users interfere with each other with a REMS gain of less than 25 dB, and (ii) the REMS gain in the direction of the secondary user is also mitigated to less than 25 dB. Both traces were calculated using (53).

to the second primary user. The REMS gain in the direction of both primary users is more than 8.5 dB. Moreover, the signals intended for the primary users interfere with each other with a REMS gain of less than 25 dB and the REMS gain in the direction of the secondary user is mitigated to less than 25 dB.

In both experiments in Figure 13 and Figure 14, the REMS gain data was calculated using (53), i.e., by applying the proposed model from Section II. To validate that our REMS gain values are correct, we also conducted a *full-wave EM simulation* of the first simulation scenario without a secondary user. In the full-wave EM simulation, we set (i) the impedance values of the reconfigurable impedances \mathbf{Z}_R and (ii) the amplitudes and phases of \mathbf{v}_{Tx} directly in the simulation software according to the output of Algorithm 1. The results from both

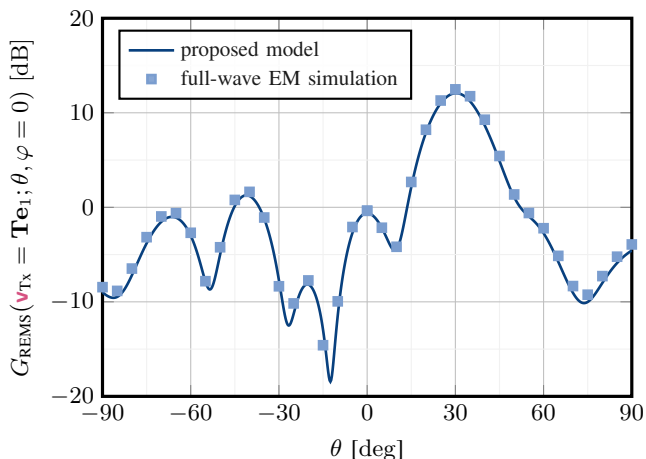


Figure 15. REMS gain G_{REMS} in the $\varphi = 0^\circ$ slice that is achieved by applying Algorithm 1 to the first simulation scenario for the case in which the secondary user is ignored. The continuous trace was calculated using the in Section II proposed modeling method with (53). The REMS gain samples shown with squares are obtained from a full-wave EM simulation. The two methods match each other.

the proposed method and the full-wave EM simulation are shown in Figure 15. As can be seen, the results from both methods match well, validating the consistency of the proposed modeling methods with physics.

V. LIMITATIONS

While the proposed modeling method is both *efficient* and *physically consistent*, it has the following key limitations.

First, Assumption 2 limits our model to REMSs with no movable parts. This prevents our model from describing systems as the ones described in [70]–[72] or so-called fluid antennas [73]. However, as movable parts tend to have a high propensity for mechanical degradation or failures, it remains an open question what role such antenna systems will play in future wireless networks.

Second, as discussed in Remark 9, we assumed that radiating structure kernels can be approximated arbitrarily well with sampled kernels. However, we have neither discussed the number of required samples nor how an optimal sampling strategy would look like. A detailed investigation of both of these aspects, which relate to the mathematical complexity of a REMS’s far field, is part of ongoing research.

Third, our proposed model in Section II is designed for a narrowband analysis of REMSs. However, our model can straightforwardly be generalized to enable a broadband analysis, for instance, by treating each frequency of interest separately. Nonetheless, it is an open question whether the model parameters for all frequencies of interest must be stored individually or if more memory- and compute-efficient approaches exist.

VI. CONCLUSIONS

In this work, we have proposed an *efficient* and *physically-consistent* modeling framework for reconfigurable electromagnetic structures (REMSs). Our rigorous mathematical formalism combines circuit-theoretic models with our REMS-to-far-field-interaction approach, which enables us to model the

interaction of arbitrary REMSs with (incoming and outgoing) electromagnetic waves in the far-field region using a *single* full-wave electromagnetic (EM) simulation. We have validated our framework in two scenarios by comparing it to Ansys HFSS simulations, which reveals the efficiency and physical accuracy of our model. In addition, we have demonstrated the effectiveness of our model via a case study of a reconfigurable reflectarray (RRA) that performs joint multiuser beam- and null-forming using a novel computationally-efficient algorithm that simultaneously optimizes the digital beamforming matrix and the RRA’s tunable parameters. All of these results confirm both the efficiency and physical consistency of our framework.

There are many avenues for future work, some of which we outline next. First, systematically investigating how the kernels of the radiating structure should be sampled is an ongoing effort. Second, while our REMS model can be generalized to performing a wideband analysis, it is currently unclear whether the model parameters for all frequencies of interest must be stored or if more efficient representations exist. Third, the algorithm proposed in Section IV-A was heuristically motivated. We believe that many refinements to our algorithm are possible, including alternative objective functions and more efficient parameter search strategies.

VII. ACKNOWLEDGMENTS

The authors would like to thank Dr. Raphael Rolny, Gian Marti, and Carolina Nolasco Ferencikova for discussions and suggestions concerning this paper. The authors also thank Prof. Hua Wang for pointing us towards reference [18] and Dr. Ali Basem for his introduction to Ansys HFSS.

The work of AST and CS was funded in part by armasuisse; the work of CS was also funded by an ETH Zurich Research Grant and by the Swiss State Secretariat for Education, Research, and Innovation (SERI) under the SwissChips initiative.

APPENDIX A PROOFS

A. Proof of Proposition 1

To prove that the outgoing far-field power wave pattern \mathbf{a}_F is an element of L^2 , we show that

$$\begin{aligned} \|\mathbf{a}_F\|_{L^2}^2 &= \lim_{r \rightarrow \infty} \iint_{\Omega} \frac{1}{Z_0} \left\| \mathbf{E}^{\nearrow}(\theta, \varphi) \right\|^2 \sin(\theta) d(\theta, \varphi) \end{aligned} \quad (82)$$

$$= \lim_{r \rightarrow \infty} \iint_{\Omega} \frac{1}{Z_0} \left\| \mathbf{E}^{\nearrow}(\theta, \varphi) \frac{e^{-jk_r r}}{r} \right\|^2 r^2 \sin(\theta) d(\theta, \varphi) \quad (83)$$

$$= P^{\nearrow}. \quad (84)$$

Here, (82) follows from Definition 3 and (13); (83) follows from incorporating the factor $\frac{e^{-jk_r r}}{r}$ to obtain the phasors of the electric fields, and (84) follows because the fields in the far-field region have plane-wave character. Because, by assumption, P^{\nearrow} is finite, it follows that $\mathbf{a}_F \in L^2$. The proof for the incoming far-field power wave pattern \mathbf{b}_F proceeds analogously. ■

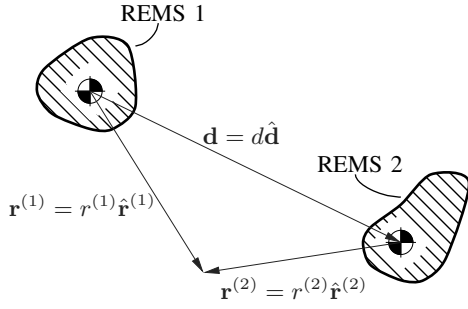


Figure 16. Two REMSs in empty space, each with the origin of a spherical coordinate system located at its center. The spatial displacement of these origins, and therefore of the REMS, is characterized by the vector \mathbf{d} , which we further factorize as the product between the distance d and the unit vector $\hat{\mathbf{d}}$. As illustrated, any point in space can be characterized by both coordinate systems using the vectors $\mathbf{r}^{(1)}$ and $\mathbf{r}^{(2)}$. Each of these position vectors can also be factorized into the scalar $r^{(\cdot)}$ and the unit vector $\hat{\mathbf{r}}^{(\cdot)}$.

B. Proof of Proposition 2

In order to apply our modeling framework to the two REMSs scenario, we utilize the two spherical coordinate systems as depicted in Figure 16. First, we derive the relationship between the outgoing far-field radiation pattern $\mathbf{a}_F^{(1)}$ of the first REMS and the incoming far-field radiation pattern $\mathbf{b}_F^{(2)}$ of the second REMS. We use the superposition principle and assume that $\mathbf{a}_F^{(2)} = \mathbf{0}$, in which case, in the far-field region of REMS 1, it holds that

$$\tilde{\mathbf{E}}^{(1)} \triangleq \begin{bmatrix} [\mathbf{E}(\mathbf{r}^{(1)})]_{\hat{\theta}^{(1)}} \\ [\mathbf{E}(\mathbf{r}^{(1)})]_{\hat{\varphi}^{(1)}} \end{bmatrix} = \sqrt{Z_0} \frac{e^{-jkr^{(1)}}}{r^{(1)}} \mathbf{a}_F^{(1)}(\hat{\mathbf{r}}^{(1)}). \quad (85)$$

We now use the relation $\mathbf{r}^{(1)} = \mathbf{r}^{(2)} + \mathbf{d}$ to rewrite (85) as follows:

$$\tilde{\mathbf{E}}^{(1)} = \sqrt{Z_0} \frac{e^{-jk\|\mathbf{r}^{(2)}+\mathbf{d}\|_2}}{\|\mathbf{r}^{(2)}+\mathbf{d}\|_2} \mathbf{a}_F^{(1)}\left(\frac{\mathbf{r}^{(2)}+\mathbf{d}}{\|\mathbf{r}^{(2)}+\mathbf{d}\|_2}\right). \quad (86)$$

Then, we utilize (i) the fact that we are interested in the case where the distance between the two REMSs approaches infinity, and (ii) the continuity assumption in the proposition, which implies that $\mathbf{a}_F^{(1)}$ is a continuous function, to conclude that

$$\lim_{d \rightarrow \infty} \tilde{\mathbf{E}}^{(1)} = \sqrt{Z_0} \frac{e^{-jkd}}{d} \mathbf{a}_F^{(1)}(\hat{\mathbf{d}}) e^{-jkr^{(2)}(\hat{\mathbf{r}}^{(2)})^T \hat{\mathbf{d}}}. \quad (87)$$

By comparing the right-hand side of (87) with (61), one can conclude that the electric field in the vicinity to the second REMS has the form of a plane wave traveling in the direction given by the unit vector $\hat{\mathbf{d}}$. It follows from (69) that, from the perspective of the second REMS, the electric field can be treated as the superposition of an incoming and an outgoing spherical wave of the form

$$\begin{aligned} \lim_{d \rightarrow \infty} \tilde{\mathbf{E}}^{(1)} &= \sqrt{Z_0} \frac{2\pi}{jk} \frac{e^{-jkd}}{d} \mathbf{a}_F^{(1)}(\hat{\mathbf{d}}) \delta(\hat{\mathbf{r}}^{(2)} + \hat{\mathbf{d}}) \frac{e^{+jkr^{(2)}}}{r^{(2)}} \\ &\quad - \sqrt{Z_0} \frac{2\pi}{jk} \frac{e^{-jkd}}{d} \mathbf{a}_F^{(1)}(\hat{\mathbf{d}}) \delta(\hat{\mathbf{r}}^{(2)} - \hat{\mathbf{d}}) \frac{e^{-jkr^{(2)}}}{r^{(2)}}. \end{aligned} \quad (88)$$

From the definition of spherical coordinates, it follows that for positions on the line between the two coordinate origins, it holds that

$$\begin{bmatrix} [\mathbf{E}(\mathbf{r}^{(2)})]_{\hat{\theta}^{(2)}} \\ [\mathbf{E}(\mathbf{r}^{(2)})]_{\hat{\varphi}^{(2)}} \end{bmatrix} = \begin{bmatrix} 1 & 0 \\ 0 & -1 \end{bmatrix} \begin{bmatrix} [\mathbf{E}(\mathbf{r}^{(1)})]_{\hat{\theta}^{(1)}} \\ [\mathbf{E}(\mathbf{r}^{(1)})]_{\hat{\varphi}^{(1)}} \end{bmatrix}. \quad (89)$$

We can now combine (88) and (89) with our definition of the far-field power wave pattern in (14) and (15) to arrive at the desired relationship

$$\lim_{d \rightarrow \infty} \mathbf{b}_F^{(2)}(\hat{\mathbf{r}}^{(2)}) = \delta(\hat{\mathbf{r}}^{(2)} + \hat{\mathbf{d}}) \mathbf{C} \mathbf{a}_F^{(1)}(\hat{\mathbf{d}}), \quad (90)$$

where we used the matrix \mathbf{C} from (46). Similarly, one can show that

$$\lim_{d \rightarrow \infty} \mathbf{b}_F^{(1)}(\hat{\mathbf{r}}^{(1)}) = \delta(\hat{\mathbf{r}}^{(1)} - \hat{\mathbf{d}}) \mathbf{C} \mathbf{a}_F^{(2)}(-\hat{\mathbf{d}}). \quad (91)$$

To complete the proof, we now assume that all circuit-theoretic ports of the radiating structures of both REMSs are perfectly matched and that only the $\ell^{(1)}$ th port of the first REMS is stimulated with a non-zero input signal. Next, we combine equations (17), (18), (20), (21), (90), and (91), and utilize the geometric series²⁶ generated by the matrix \mathbf{M} from (46) to arrive at

$$\begin{aligned} \lim_{d \rightarrow \infty} [\mathbf{b}_R^{(2)}]_{\ell^{(2)}} &= \left(\mathbf{s}_{\text{RRF}}^{(2)}(\ell^{(2)}; -\hat{\mathbf{d}}) \right)^T \mathbf{C} (\mathbf{I}_2 - \mathbf{M})^{-1} \\ &\quad \cdot \mathbf{s}_{\text{RRF}}^{(1)}(\ell^{(1)}; \hat{\mathbf{d}}) [\mathbf{a}_R^{(1)}]_{\ell^{(1)}}, \end{aligned} \quad (92)$$

which concludes the proof. \blacksquare

C. Proof of Proposition 3

By construction, the volume V_R depicted in Figure 7 contains no sources. Because we furthermore assume Lorentz reciprocity holds for the volume V_R as $R \rightarrow \infty$, it follows by definition that (54) holds for $V = V_R$ when R is sufficiently large. We divide the surface ∂V_R into S_R and $S_{\text{port},m}$, $\tilde{S}_{\text{port},m}$ for $m \in [M]$ as depicted in Figure 7. Consequently, one can write

$$0 W = \lim_{R \rightarrow \infty} \iint_{\partial V_R} \hat{\mathbf{n}}^T (\mathbf{E}_1 \times \mathbf{H}_2 - \mathbf{E}_2 \times \mathbf{H}_1) dS \quad (93)$$

$$\begin{aligned} &= \lim_{R \rightarrow \infty} \iint_{S_R} \hat{\mathbf{r}}^T (\mathbf{E}_1 \times \mathbf{H}_2 - \mathbf{E}_2 \times \mathbf{H}_1) dS \\ &\quad + \sum_{m \in [M]} \iint_{S_{\text{port},m}} \hat{\mathbf{n}}_m^T (\mathbf{E}_1 \times \mathbf{H}_2 - \mathbf{E}_2 \times \mathbf{H}_1) dS \\ &\quad + \sum_{m \in [M]} \iint_{\tilde{S}_{\text{port},m}} \hat{\mathbf{n}}^T (\mathbf{E}_1 \times \mathbf{H}_2 - \mathbf{E}_2 \times \mathbf{H}_1) dS, \end{aligned} \quad (94)$$

$= 0 W / m^2$

where the last term can be deduced because, inside a perfectly conducting shield, the electric field strength is equal to zero. We now analyze the two remaining integral and sum terms in (94) separately. It holds that

$$\lim_{R \rightarrow \infty} \iint_{S_R} \hat{\mathbf{r}}^T (\mathbf{E}_1 \times \mathbf{H}_2 - \mathbf{E}_2 \times \mathbf{H}_1) dS$$

²⁶This geometric series converges for sufficiently large distances d , as both singular values of \mathbf{M} approach 0 for $d \rightarrow \infty$. Consequently, the inverse of $\mathbf{I} - \mathbf{M}$ is guaranteed to exist.

$$= -\frac{2}{Z_0} \iint_{\Omega} \left(\mathbf{E}_1^{\leftarrow} \right)^{\top} \mathbf{E}_2^{\rightarrow} - \left(\mathbf{E}_2^{\leftarrow} \right)^{\top} \mathbf{E}_1^{\rightarrow} d\Omega \quad (95)$$

$$= -2 \iint_{\Omega} \left(\mathbf{b}_F^{(1)} \right)^{\top} \mathbf{a}_F^{(2)} - \left(\mathbf{b}_F^{(2)} \right)^{\top} \mathbf{a}_F^{(1)} d\Omega. \quad (96)$$

Here, (95) follows from the Maxwell-Faraday equation $\nabla \times \mathbf{E} = -j\omega\mu\mathbf{H}$ and the fact that for large R , the electric field on S_R can be written as a decomposition into an outgoing and an incoming wave, as in (12). Equation (96) follows directly from (14) and (15).

We mainly follow the derivation in [48, Ch. 1, Sec. 4], using our definition of power waves in (1) and (2), along with the assumption that each port supports exactly one propagation mode, to derive that

$$\sum_{m \in [M]} \iint_{S_{\text{port}, m}} \hat{\mathbf{n}}_m \cdot (\mathbf{E}_1 \times \mathbf{H}_2 - \mathbf{E}_2 \times \mathbf{H}_1) dS$$

$$= -2 \sum_{m \in [M]} \mathbf{a}_{R,m}^{(1)} \mathbf{b}_{R,m}^{(2)} - \mathbf{a}_{R,m}^{(2)} \mathbf{b}_{R,m}^{(1)} \quad (97)$$

$$= -2 \left(\left(\mathbf{a}_R^{(1)} \right)^{\top} \mathbf{b}_R^{(2)} - \left(\mathbf{a}_R^{(2)} \right)^{\top} \mathbf{b}_R^{(1)} \right). \quad (98)$$

By inserting (96) and (98) back into (94), we arrive at

$$\iint_{\Omega} \left(\mathbf{b}_F^{(1)} \right)^{\top} \mathbf{a}_F^{(2)} - \left(\mathbf{b}_F^{(2)} \right)^{\top} \mathbf{a}_F^{(1)} d\Omega = \left(\mathbf{b}_R^{(1)} \right)^{\top} \mathbf{a}_R^{(2)} - \left(\mathbf{b}_R^{(2)} \right)^{\top} \mathbf{a}_R^{(1)}. \quad (99)$$

Since the incoming waves \mathbf{b}_R and \mathbf{b}_F can be chosen arbitrarily and the corresponding outgoing waves \mathbf{a}_R and \mathbf{a}_F are fully determined by (17), (18), (20), and (21), it holds that

$$0 W = \left(\mathbf{a}_R^{(1)} \right)^{\top} \left(\mathbb{S}_{\text{RRR}} - \mathbb{S}_{\text{RRR}}^{\top} \right) \mathbf{a}_R^{(2)} \quad (100)$$

$$0 W = \sum_{m \in [M]} \mathbf{a}_{R,m}^{(2)} \langle \mathbf{b}_F^{(1)}, \bar{\mathbb{S}}_{\text{RFR}}(m; \cdot) - \bar{\mathbb{S}}_{\text{RFR}}(m; \cdot) \rangle_{L^2} \quad (101)$$

$$0 W = \iint_{\Omega} \iint_{\Omega'} \left(\mathbf{b}_F^{(2)}(\hat{\mathbf{r}}) \right)^{\top} \left(\mathbb{S}_{\text{RFF}}(\hat{\mathbf{r}}; \hat{\mathbf{r}}') - \mathbb{S}_{\text{RFF}}^{\top}(\hat{\mathbf{r}}'; \hat{\mathbf{r}}) \right) \mathbf{b}_R^{(1)}(\hat{\mathbf{r}}') d\Omega' d\Omega. \quad (102)$$

Here, (100) follows from setting $\mathbf{b}_F^{(1)}$ and $\mathbf{b}_F^{(2)}$ to zero, (101) follows from setting $\mathbf{a}_R^{(1)}$ and $\mathbf{b}_F^{(2)}$ to zero, and (102) follows from setting $\mathbf{a}_R^{(1)}$ and $\mathbf{a}_R^{(2)}$ to zero. Finally, we use the fact that \mathbf{a}_R and \mathbf{b}_F can be chosen arbitrarily to conclude from (100), (101), and (102) that the Proposition holds. ■

D. Proof of Equation (18)

Since \mathbb{S}_{RFR} is a finite-rank operator with rank not larger than M , it can be represented using the following canonical form of finite-rank operators (cf. [74, Thm. 6.1]):

$$\mathbb{S}_{\text{RFR}} \mathbf{v} = \sum_{n \in [M]} \alpha_n \langle \mathbf{v}, \mathbf{g}_n \rangle \tilde{\mathbf{g}}_n. \quad (103)$$

Here, $\{\mathbf{g}_n\}_{n \in [M]}$, $\mathbf{g}_n \in \mathbb{C}^M$ and $\{\tilde{\mathbf{g}}_n\}_{n \in [M]}$, $\tilde{\mathbf{g}}_n \in L^2$ are orthonormal bases, and $\{\alpha_n\}_{n \in [M]}$ are coefficients in \mathbb{C} . We now expand each element \mathbf{g}_n into the standard basis of \mathbb{R}^M , denoted by $\{\mathbf{e}_m\}_{m \in [M]}$, and write

$$\left(\mathbb{S}_{\text{RFR}} \mathbf{v} \right) (\theta, \varphi) = \sum_{n \in [M]} \alpha_n \langle \mathbf{v}, \mathbf{g}_n \rangle \tilde{\mathbf{g}}_n(\theta, \varphi)$$

$$= \sum_{n \in [M]} \alpha_n \left\langle \mathbf{v}, \sum_{m \in [M]} \langle \mathbf{g}_n, \mathbf{e}_m \rangle \mathbf{e}_m \right\rangle \tilde{\mathbf{g}}_n(\theta, \varphi) \quad (104)$$

$$= \sum_{m \in [M]} \sum_{n \in [M]} \alpha_n \langle \mathbf{v}, \mathbf{e}_m \rangle \overline{\langle \mathbf{g}_n, \mathbf{e}_m \rangle} \tilde{\mathbf{g}}_n(\theta, \varphi) \quad (105)$$

$$= \sum_{m \in [M]} \underbrace{\sum_{n \in [M]} \alpha_n \overline{\langle \mathbf{g}_n \rangle_m} \tilde{\mathbf{g}}_n(\theta, \varphi)}_{\triangleq \mathbb{S}_{\text{RFR}}(m; \theta, \varphi)} [\mathbf{v}]_m, \quad (106)$$

where we perform the above-mentioned extension to obtain (104). Here, (105) is a consequence of the linearity characteristics of inner products and where (106) simply involves reordering terms. ■

E. Proof of Equation (20)

We exploit that \mathbb{S}_{RFR} is a finite-rank operator with rank not larger than M . Therefore we can represent the operator using the following canonical form of finite-rank operators (cf. [74, Thm. 6.1]):

$$\left[\mathbb{S}_{\text{RFR}} \mathbf{f} \right]_m = \left[\sum_{n \in [M]} \alpha_n \langle \mathbf{f}, \tilde{\mathbf{g}}_n \rangle \mathbf{g}_n \right]_m \quad (107)$$

with $m \in [M]$. Here, $\{\mathbf{g}_n\}_{n \in [M]}$, $\mathbf{g}_n \in \mathbb{C}^M$ and $\{\tilde{\mathbf{g}}_n\}_{n \in [M]}$, $\tilde{\mathbf{g}}_n \in L^2$ are orthonormal bases and $\{\alpha_n\}_{n \in [M]}$ are coefficients in \mathbb{C} . We now expand each element \mathbf{g}_n into the standard basis of \mathbb{R}^M , denoted by $\{\mathbf{e}_{m'}\}_{m' \in [M]}$, and write

$$\left[\mathbb{S}_{\text{RFR}} \mathbf{f} \right]_m = \left[\sum_{n \in [M]} \alpha_n \langle \mathbf{f}, \tilde{\mathbf{g}}_n \rangle_{L^2} \mathbf{g}_n \right]_m$$

$$= \left[\sum_{n \in [M]} \alpha_n \langle \mathbf{f}, \tilde{\mathbf{g}}_n \rangle_{L^2} \sum_{m' \in [M]} \langle \mathbf{g}_n, \mathbf{e}_{m'} \rangle_{\mathbb{C}^M} \mathbf{e}_{m'} \right]_m \quad (108)$$

$$= \sum_{n \in [M]} \alpha_n \langle \mathbf{f}, \tilde{\mathbf{g}}_n \rangle_{L^2} [\mathbf{g}_n]_m \quad (109)$$

$$= \langle \mathbf{f}, \underbrace{\sum_{n \in [M]} \overline{\langle \mathbf{g}_n \rangle_m} \tilde{\mathbf{g}}_n}_{\triangleq \bar{\mathbb{S}}_{\text{RFR}}(m; \theta, \varphi)} \rangle_{L^2}, \quad (110)$$

where we perform the above-mentioned extension to obtain (108); where (109) follows from the filter characteristics of the standard basis; and where (110) is a consequence of the linearity characteristics of inner products. ■

F. Proof of Right-Hand Side Equalities in Definition 5

It follows from Definition 5 and the definition of power waves in (1) and (2) that

$$P_{\text{T}} \triangleq \Re \{ \mathbf{v}_{\text{T}}^H \mathbf{i}_{\text{T}} \} \quad (111)$$

$$= \Re \{ \sqrt{R_0} (\mathbf{a}_{\text{T}} + \mathbf{b}_{\text{T}})^H (\sqrt{R_0})^{-1} (\mathbf{a}_{\text{T}} - \mathbf{b}_{\text{T}}) \} \quad (112)$$

$$= \Re \{ (\mathbf{a}_{\text{T}} + \mathbf{b}_{\text{T}})^H (\mathbf{a}_{\text{T}} - \mathbf{b}_{\text{T}}) \} \quad (113)$$

$$= \|\mathbf{a}_{\text{T}}\|_2^2 - \|\mathbf{b}_{\text{T}}\|_2^2 + \Re \{ 2j \Im \{ \mathbf{b}_{\text{T}}^H \mathbf{a}_{\text{T}} \} \} \quad (114)$$

$$= \|\mathbf{a}_{\text{T}}\|_2^2 - \|\mathbf{b}_{\text{T}}\|_2^2. \quad (115)$$

The right-hand side of (49) can be proven analogously, and the right-hand side of (50) follows directly from the proof of Proposition 1. ■

G. Proof of Right-Hand Side Equality in Definition 6

Let $\mathbf{v}_\Gamma = \mathbf{0}$, $\mathbf{i}_\Gamma = \mathbf{0}$, $\mathbf{v}_\Upsilon = \mathbf{0}$, and $\mathbf{b}_F = \mathbf{0}$. We will now demonstrate that the term P_T is upper bounded by

$$P_T = \sum_{n \in [N]} \Re\{\mathbf{v}_{T,n} \mathbf{i}_{T,n}\} = \sum_{n \in [N_{Tx}]} \Re\{\mathbf{v}_{T,n} \mathbf{i}_{T,n}\} \quad (116)$$

$$= \sum_{n \in [N_{Tx}]} \frac{1}{4\Re\{\mathbf{Z}_{Tx,n}\}} \left(|\mathbf{v}_{T,n} + \mathbf{Z}_{Tx,n} \mathbf{i}_{T,n}|^2 - |\mathbf{v}_{T,n} - \mathbf{Z}_{Tx,n} \mathbf{i}_{T,n}|^2 \right) \quad (117)$$

$$\leq \sum_{n \in [N_{Tx}]} \frac{1}{4\Re\{\mathbf{Z}_{Tx,n}\}} |\mathbf{v}_{T,n} + \mathbf{Z}_{Tx,n} \mathbf{i}_{T,n}|^2 \quad (118)$$

$$= \sum_{n \in [N_{Tx}]} \frac{1}{4} \overline{(\mathbf{v}_{T,n} + \mathbf{Z}_{Tx,n} \mathbf{i}_{T,n})} \Re\{\mathbf{Z}_{Tx,n}\}^{-1} (\mathbf{v}_{T,n} + \mathbf{Z}_{Tx,n} \mathbf{i}_{T,n}) \quad (119)$$

$$= \sum_{n \in [N_{Tx}]} \frac{1}{4} \overline{\mathbf{v}_{Tx,n}} \Re\{\mathbf{Z}_{Tx,n}\}^{-1} \mathbf{v}_{Tx,n} \quad (120)$$

$$= \frac{1}{4} \mathbf{v}_{Tx}^H \Re\{\mathbf{Z}_{Tx}\}^{-1} \mathbf{v}_{Tx}. \quad (121)$$

Here, the second equality in (116) follows from the fact that the LNA blocks are passive systems, as we assumed that $\mathbf{v}_\Gamma = \mathbf{0}$ and $\mathbf{i}_\Gamma = \mathbf{0}$, and (118) follows from Assumption 1. To show that the bound in (121) is tight, we now demonstrate that

$$\text{for } \mathbf{S}_T = \begin{bmatrix} \mathbf{S}_{T_{TT}}^{\text{Tx}} & \mathbf{0} \\ \mathbf{0} & \mathbf{0} \end{bmatrix}$$

and $\mathbf{S}_{T_{TT}}^{\text{Tx}} = (\overline{\mathbf{Z}}_{Tx} + R_0 \mathbf{I}_N)^{-1} (\overline{\mathbf{Z}}_{Tx} - R_0 \mathbf{I}_N)$, it holds that

$$P_T = \Re\{\mathbf{v}_T^H \mathbf{i}_T\} \quad (122)$$

$$= \Re\{(\overline{\mathbf{Z}}_{Tx} \mathbf{i}_T)^H \mathbf{i}_T\} \quad (123)$$

$$= \frac{1}{4} \Re\{(\overline{\mathbf{Z}}_{Tx} \Re\{\mathbf{Z}_{Tx}\}^{-1} \mathbf{v}_{Tx})^H \Re\{\mathbf{Z}_{Tx}\}^{-1} \mathbf{v}_{Tx}\} \quad (124)$$

$$= \frac{1}{4} \mathbf{v}_{Tx}^H \Re\{\mathbf{Z}_{Tx}\}^{-1} \mathbf{v}_{Tx}, \quad (125)$$

where (122) follows from recognizing that, for the chosen scattering matrix \mathbf{S}_T , the input impedance of the tuning network seen by the PAs is equal to $\overline{\mathbf{Z}}_{Tx}$. This concludes the proof. ■

REFERENCES

- [1] D. Dardari, "Dynamic scattering arrays for simultaneous electromagnetic processing and radiation in holographic MIMO systems," May 2024, *arXiv: 2405.16174v1*.
- [2] Y. Hao, C. Deng, X. Cao, Y. Yin, and K. Sarabandi, "A high aperture efficiency 1-bit reconfigurable reflectarray antenna with extremely low power consumption," *IEEE Trans. Antennas Propag.*, vol. 72, no. 1, pp. 1015–1020, Jan. 2024.
- [3] N. Zhang, K. Chen, J. Zhao, Q. Hu, K. Tang, J. Zhao, T. Jiang, and Y. Feng, "A dual-polarized reconfigurable reflectarray antenna based on dual-channel programmable metasurface," *IEEE Trans. Antennas Propag.*, vol. 70, no. 9, pp. 7403–7412, Sep. 2022.
- [4] V. Jamali, A. M. Tulino, G. Fischer, R. R. Müller, and R. Schober, "Intelligent surface-aided transmitter architectures for millimeter-wave ultra massive MIMO systems," *IEEE Open J. Commun. Soc.*, vol. 2, pp. 144–167, Dec. 2020.
- [5] H. Yang, F. Yang, S. Xu, Y. Mao, M. Li, X. Cao, and J. Gao, "A 1-bit 10×10 reconfigurable reflectarray antenna: Design, optimization, and experiment," *IEEE Trans. Antennas Propag.*, vol. 64, no. 6, pp. 2246–2254, Jun. 2016.
- [6] S. V. Hum and J. Perruisseau-Carrier, "Reconfigurable reflectarrays and array lenses for dynamic antenna beam control: A review," *IEEE Trans. Antennas Propag.*, vol. 62, no. 1, pp. 183–198, Jan. 2012.
- [7] X. Cao, C. Deng, Y. Yin, Y. Hao, and K. Sarabandi, "1-bit reconfigurable transmit- and reflect-array antenna using patch-ground-patch structure," *IEEE Antennas Wireless Propag. Lett.*, vol. 23, no. 1, pp. 434–438, Jan. 2024.
- [8] S. Venkatesh, X. Lu, H. Saeidi, and K. Sengupta, "A high-speed programmable and scalable terahertz holographic metasurface based on tiled CMOS chips," *Nat. Electron.*, vol. 3, p. 785–793, Dec. 2020.
- [9] J. Y. Lau and S. V. Hum, "Reconfigurable transmitarray design approaches for beamforming applications," *IEEE Trans. Antennas Propag.*, vol. 60, no. 12, pp. 5679–5689, Dec. 2012.
- [10] M. Di Renzo, A. Zappone, M. Debbah, M. S. Alouini, C. Yuen, J. de Rosny, and S. Tretyakov, "Smart radio environments empowered by reconfigurable intelligent surfaces: How it works, state of research, and the road ahead," *IEEE J. Sel. Areas Commun.*, vol. 38, no. 11, pp. 2450–2525, Nov. 2020.
- [11] Q. Wu, S. Zhang, B. Zheng, C. You, and R. Zhang, "Intelligent reflecting surface-aided wireless communications: A tutorial," *IEEE Trans. Commun.*, vol. 69, no. 5, pp. 3313–3351, May 2021.
- [12] Q. Wu, B. Zheng, C. You, L. Zhu, K. Shen, X. Shao, W. Mei, B. Di, H. Zhang, E. Basar, L. Song, M. Di Renzo, Z. Q. Luo, and R. Zhang, "Intelligent surfaces empowered wireless network: Recent advances and the road to 6G," *Proc. IEEE*, vol. 112, no. 7, pp. 724–763, Jul. 2024.
- [13] J. An, C. Yuen, L. Guan, M. Di Renzo, M. Debbah, H. V. Poor, and L. Hanzo, "Two-dimensional direction-of-arrival estimation using stacked intelligent metasurfaces," *IEEE J. Sel. Areas Commun.*, vol. 42, no. 10, pp. 2786–2802, Oct. 2024.
- [14] J. An, M. Di Renzo, M. Debbah, and C. Yuen, "Stacked intelligent metasurfaces for multiuser beamforming in the wave domain," in *Proc. IEEE Int. Conference Commun. (ICC)*, Rome, Italy, May 2023, pp. 2834–2839.
- [15] H. Zhang, H. Zhang, B. Di, M. Di Renzo, Z. Han, H. V. Poor, and L. Song, "Holographic integrated sensing and communication," *IEEE J. Sel. Areas Commun.*, vol. 40, no. 7, pp. 2114–2130, Jul. 2022.
- [16] L. Zhang, M. Z. Chen, W. Tang, J. Y. Dai, L. Miao, X. Y. Zhou, S. Jin, Q. Cheng, and T. J. Cui, "A wireless communication scheme based on space- and frequency-division multiplexing using digital metasurfaces," *Nat. Electron.*, vol. 4, pp. 218–227, Mar. 2021.
- [17] C. Huang, C. Zhang, J. Yang, B. Sun, B. Zhao, and X. Luo, "Reconfigurable metasurface for multifunctional control of electromagnetic waves," *Adv. Optical Mater.*, vol. 5, no. 22, Sep. 2017.
- [18] A. Babakhani, D. B. Rutledge, and A. Hajimiri, "Transmitter architectures based on near-field direct antenna modulation," *IEEE J. Solid-State Circuits*, vol. 43, no. 12, pp. 2674–2692, Dec. 2008.
- [19] H. R. Zu, B. Wu, W. H. Li, T. Su, Y. Liu, W. X. Tang, D. P. He, and T. J. Cui, "Optically and radiofrequency-transparent metadevices based on quasi-one-dimensional surface plasmon polariton structures," *Nat. Electron.*, vol. 6, pp. 525–533, Jul. 2023.
- [20] Z. Shao, R. Shen, W. Xia, Y. Ghasempour, K. Sengupta, and S. Rangan, "A hybrid antenna-metasurface architecture for mmWave and THz massive MIMO," in *Proc. IEEE Conf. Rec. Asilomar Conf. Signals, Sys., and Comp.*, Pacific Grove, CA, USA, Oct. 2023, pp. 1610–1615.
- [21] P. Naseri, M. Riel, Y. Demers, and S. V. Hum, "A dual-band dual-circularly polarized reflectarray for K/Ka-band space applications," *IEEE Trans. Antennas Propag.*, vol. 68, no. 6, pp. 4627–4637, Jun. 2020.
- [22] D. Martinez-de-Rioja, E. Martinez-de-Rioja, and J. A. Encinar, "Preliminary simulations of a 1.8-m reflectarray antenna in a geostationary satellite to generate multi-spot coverage," in *Proc. IEEE Eur. Conf. Antennas Propag. (EuCAP)*, Krakow, Poland, Mar. 2019, pp. 1–5.
- [23] Ansys HFSS 2022 R1. Ansys, Inc.
- [24] W. Tang, X. Chen, M. Z. Chen, J. Y. Dai, Y. Han, M. Di Renzo, Y. Zeng, S. Jin, Q. Cheng, and T. J. Cui, "Wireless communications with reconfigurable intelligent surface: Path loss modeling and experimental measurement," *IEEE Trans. Wireless Commun.*, vol. 20, no. 1, pp. 421–439, Jan. 2021.
- [25] Ö. T. Demir and E. Björnson, "User-centric cell-free massive mimo with RIS-integrated antenna arrays," Sep. 2024, *arXiv: 2409.15765v1*.
- [26] K. K. Tiwari and G. Caire, "A new old idea: Beam-steering reflectarrays for efficient sub-THz multiuser MIMO," Dec. 2023, *arXiv: 2311.18593v2*.
- [27] Y. Cui and H. Yin, "Channel estimation for RIS-aided mmWave communications via 3D positioning," in *Proc. IEEE Int. Conf. Commun. China (ICCC)*, Xiamen, China, 2021, pp. 399–404.

- [28] Ö. Özdoğan, E. Björnson, and E. G. Larsson, "Intelligent reflecting surfaces: Physics, propagation, and pathloss modeling," *IEEE Wireless Commun. Lett.*, vol. 9, no. 5, pp. 581–585, May 2020.
- [29] L. Li and T. J. Cui, "Information metamaterials – from effective media to real-time information processing systems," *Nanophotonics*, vol. 8, no. 5, pp. 703–704, Mar. 2019.
- [30] M. Moccia, S. Liu, R. Y. Wu, G. Castaldi, A. Andreone, T. J. Cui, and V. Galdi, "Coding metasurfaces for diffuse scattering: Scaling laws, bounds, and suboptimal design," *Adv. Optical Mater.*, vol. 5, no. 19, Mar. 2017.
- [31] M. W. Shabir, M. Di Renzo, A. Zappone, and M. Debbah, "Electromagnetically consistent optimization algorithms for the global design of RIS," Sep. 2024, *arXiv: 2409.17295v1*.
- [32] M. Di Renzo, F. H. Danufane, and S. Tretjakov, "Communication models for reconfigurable intelligent surfaces: From surface electromagnetics to wireless networks optimization," *Proc. IEEE*, vol. 110, no. 9, pp. 1164–1209, Sep. 2022.
- [33] M. Johnson, P. Bowen, N. Kundtz, and A. Bily, "Discrete-dipole approximation model for control and optimization of a holographic metamaterial antenna," *Appl. Opt.*, vol. 53, no. 25, pp. 5791–5799, Sep. 2014.
- [34] A. V. Diebold, D. Pande, C. Gregg, and D. R. Smith, "Reflectarray design using a discrete dipole framework," *IEEE Open J. Antennas Propag.*, vol. 4, pp. 216–228, Feb. 2023.
- [35] L. Han, H. Yin, and T. L. Marzetta, "Coupling matrix-based beamforming for superdirective antenna arrays," in *Proc. IEEE Int. Conference Commun. (ICC)*, Seoul, Korea, May 2022, pp. 5159–5164.
- [36] R. Ji, C. Huang, X. Chen, W. E. I. Sha, L. Dai, J. He, Z. Zhang, C. Yuen, and M. Debbah, "Electromagnetic hybrid beamforming for holographic MIMO communications," Oct. 2024, *arXiv: 2403.05970v2*.
- [37] J. W. Wallace and M. A. Jensen, "Mutual coupling in MIMO wireless systems: A rigorous network theory analysis," *IEEE Trans. Wireless Commun.*, vol. 3, no. 4, pp. 1317–1325, Jul. 2004.
- [38] M. T. Ivrlač and J. A. Nossek, "Toward a circuit theory of communication," *IEEE Trans. Circuits Syst. I*, vol. 57, no. 7, pp. 1663–1683, Jul. 2010.
- [39] G. Gradoni and M. Di Renzo, "End-to-end mutual coupling aware communication model for reconfigurable intelligent surfaces: An electromagnetic-compliant approach based on mutual impedances," *IEEE Wireless Commun. Lett.*, vol. 10, no. 5, pp. 938–942, May 2021.
- [40] M. Nerini, G. Gradoni, and B. Clerckx, "Physics-compliant modeling and scaling laws of multi-RIS aided MIMO systems," Nov. 2024, *arXiv: 2411.06309v1*.
- [41] H. Li and B. Clerckx, "Non-reciprocal beyond diagonal RIS: Multiport network models and performance benefits in full-duplex systems," Nov. 2024, *arXiv: 2411.04370v1*.
- [42] M. Nerini, S. Shen, H. Li, M. Di Renzo, and B. Clerckx, "A universal framework for multiport network analysis of reconfigurable intelligent surfaces," *IEEE Trans. Wireless Commun.*, vol. 23, no. 10, pp. 14 575–14 590, Oct. 2024.
- [43] J. A. Nossek, D. Semmler, M. Joham, and W. Utschick, "Physically consistent modeling of wireless links with reconfigurable intelligent surfaces using multiport network analysis," *IEEE Wireless Commun. Lett.*, vol. 13, no. 8, pp. 2240–2244, Aug. 2024.
- [44] M. Nerini and B. Clerckx, "Physically consistent modeling of stacked intelligent metasurfaces implemented with beyond diagonal RIS," *IEEE Commun. Lett.*, vol. 28, no. 7, pp. 1693–1697, Jul. 2024.
- [45] N. Balasuriya, A. Mezghani, and E. Hossain, "Physically-consistent multi-band massive MIMO systems: A radio resource management model," Jul. 2024, *arXiv: 2407.20945v1*.
- [46] P. del Hougne, "Physics-compliant diagonal representation of beyond-diagonal RIS," Jul. 2024, *arXiv: 2403.17222*.
- [47] S. Shen, B. Clerckx, and R. Murch, "Modeling and architecture design of reconfigurable intelligent surfaces using scattering parameter network analysis," *IEEE Trans. Wireless Commun.*, vol. 21, no. 2, pp. 1229–1243, Feb. 2022.
- [48] D. M. Kerns, *Plane-Wave Scattering-Matrix Theory of Antennas and Antenna-Antenna Interactions*. Washington, D.C., USA: U.S. Government Printing Office, 1981.
- [49] R. L. Lewis, *Spherical-Wave Source-Scattering Matrix Analysis of Antennas and Antenna-Antenna Interactions*. Washington, D.C., USA: U.S. Government Printing Office, 1995.
- [50] J. E. Hansen, *Spherical Near-field Antenna Measurements*, 3rd ed. London, UK: The Institution of Engineering and Technology, 2008.
- [51] C. Shi, J. Pan, X. Gu, S. Liang, and L. Zuo, "Generalized scattering matrix of antenna: Moment solution, compression storage and application," Oct. 2024, *arXiv: 2411.08904v1*.
- [52] M. Nietro-Vesperinas, *Scattering and Diffraction in Physical Optics*, 2nd ed. Singapore: World Scientific, 2006.
- [53] A. Mezghani, F. Bellili, and E. Hossain, "Reconfigurable intelligent surfaces for quasi-passive mmWave and THz networks: Should they be reflective or redirective?" in *Proc. IEEE Conf. Rec. Asilomar Conf. Signals, Sys., and Comp.*, Pacific Grove, CA, USA, Oct. 2022, pp. 1076–1080.
- [54] D. Wijekoon, A. Mezghani, G. C. Alexandropoulos, and E. Hossain, "Physically-consistent modeling and optimization of non-local RIS-assisted multi-user MIMO communication systems," Jun. 2024, *arXiv: 2406.05617v1*.
- [55] A. Mezghani, M. Akrouf, M. R. Castellanos, S. Saab, B. Hochwald, R. W. H. Jr., and J. A. Nossek, "Reincorporating circuit theory into information theory," *IEEE BITS Inf. Theory Mag.*, early access, Dec. 25, 2023, doi: 10.1109/MBITS.2023.3346329.
- [56] D. M. Kerns and E. S. Dayhoff, "Theory of diffraction in microwave interferometry," *J. Res. Natl. Inst. Stand. Technol.*, vol. 64B, no. 1, pp. 1–13, Jan. 1960.
- [57] J. Engberg and T. Larsen, *Noise Theory of Linear and Nonlinear Circuits*, 1st ed. Hoboken, NJ, USA: Wiley, 1995.
- [58] D. M. Pozar, *Microwave Engineering*, 4th ed. Hoboken, NJ, USA: Wiley, 2011.
- [59] K. Kurokawa, "Power waves and the scattering matrix," *IEEE Trans. Microw. Theory Tech.*, vol. 13, no. 2, pp. 194–202, Mar. 1965.
- [60] *Quantities and units Part 2: Mathematics*, ISO 80000-2, 2019.
- [61] R. C. Jones, "A new calculus for the treatment of optical systems. I." *J. Opt. Soc. Am.*, vol. 32, no. 8, pp. 486–493, Mar. 1942.
- [62] F. L. Pedrotti, L. M. Pedrotti, and L. S. Pedrotti, *Introduction to Optics*, 3rd ed. Boston, MA, USA: Addison Wesley, 2006.
- [63] D. S. Saxon, "Tensor scattering matrix for the electromagnetic field," *Phys. Rev.*, vol. 100, no. 6, pp. 1771–1775, Aug. 1955.
- [64] D. Riegle and P. Lin, "Matrix signal flow graphs and an optimum topological method for evaluating their gains," *IEEE Trans. Circuit Theory*, vol. 19, no. 5, pp. 427–435, Sep. 1972.
- [65] C. A. Balanis, *Antenna Theory*, 2nd ed. Hoboken, NJ, USA: Wiley, 1997.
- [66] O. M. Bucci and G. Franceschetti, "On the spatial bandwidth of scattered fields," *IEEE Trans. Antennas Propag.*, vol. 35, no. 12, pp. 1445–1455, Dec. 1987.
- [67] E. Björnson, J. Hoydis, and L. Sanguinetti, *Massive MIMO Networks: Spectral, Energy, and Hardware Efficiency*. Boston, MA, USA: now, 2017.
- [68] D. P. Bertsekas, *Nonlinear Programming*, 3rd ed. Belmont, MA, USA: Athena Scientific, 2016.
- [69] MCE Metelics, "GaAs hyperabrupt tuning varactors," MGV-100-21 datasheet, [Revised Nov. 2002].
- [70] C. Lor, R. Phon, and S. Lim, "Reconfigurable transmissive metasurface with a combination of scissor and rotation actuators for independently controlling beam scanning and polarization conversion," *Nat. Microsyst. Nanoeng.*, vol. 10, pp. 1–8, Nov. 2024.
- [71] M. Veljovic and A. K. Skrivervik, "Ultralow-profile circularly polarized reflectarray antenna for cubesat intersatellite links in K-band," *IEEE Trans. Antennas Propag.*, vol. 69, no. 8, pp. 4588–4597, Aug. 2021.
- [72] J. Huang and R. J. Pogorzelski, "A Ka-band microstrip reflectarray with elements having variable rotation angles," *IEEE Trans. Antennas Propag.*, vol. 46, no. 5, pp. 650–656, May 1998.
- [73] K. K. Wong, A. Shojaeifard, K. F. Tong, and Y. Zhang, "Fluid antenna systems," *IEEE Trans. Wireless Commun.*, vol. 20, no. 3, pp. 1950–1962, Mar. 2021.
- [74] J. Weidmann, *Linear Operators in Hilbert Spaces*, 1st ed., ser. Graduate Texts in Mathematics, 68. New York, NY, USA: Springer, 1980.